

OBSERVING SYSTEM SIMULATION EXPERIMENTS ON THE OAH'U
REGIONAL OCEAN MODEL

A THESIS SUBMITTED TO THE GRADUATE DIVISION OF THE
UNIVERSITY OF HAWAI'I AT MĀNOA IN PARTIAL FULFILLMENT
OF THE REQUIREMENTS FOR THE DEGREE OF

MASTER OF SCIENCE

IN

OCEANOGRAPHY

MAY 2011

By

Rebecca E. Baltes

Thesis Committee:

Brian S. Powell, Chairperson

Pierre Flament

Glenn S. Carter

© Copyright by
Rebecca E. Baltes
2011

Acknowledgements

Thank you to Dr. Brian Powell, my advisor. Thank you for your guidance, patience and support. Thank you for your many hours spent teaching me about modeling, programming and learning how to think through and process problems as an oceanographer.

Thank you to Dr. Pierre Flament for your assistance during my transition in projects as well as for serving on my advisory committee. Thank you to Dr. Glenn Carter for serving on my committee as well as for all the help learning how to code efficiently in Matlab. Thank you to Dr. Mark Merrifield for patiently teaching me how to analyze data quantitatively and interpret the results of the analysis.

Thank you to all the members of Brian's lab, who taught me tools and tricks of the trade. Thanks to all my fellow students who helped me along the way with course work and research, especially Assaf Azouri, Jake Cass, and Saulo Soares. Most especially, thank you to KR and my family, whose incredible support made this possible.

Abstract

Observing system simulation experiments were conducted using the Oah'u Regional Ocean Modeling System. A twin experiment was implemented in which synthetic observing systems were withheld to establish the impact of each observing system on 4-day ocean forecasts over a 6 month experiment period. Synthetic High Frequency(HF) Radar had significant impacts on the forecasts across the region. It provided a surface velocity constraint that influenced forecasts at depth and in areas of the region not directly surveyed by HF Radar. Additional analyses of the observing systems were conducted at the outflow plume depth of a potential pilot Ocean Thermal Energy Conversion (OTEC) site off the south coast of Oah'u as well as the circulation of Mamala Bay. Synthetic satellite data had a positive impact on the temperature forecasts, especially in the island wake area, west of Oah'u. Glider data from continuous synthetic runs between Makapu'u and Penguin Banks and data from a synthetic mooring stationed in the deepest part of the Ka'iwi Channel constrained the model well in the Ka'iwi Channel. They both showed positive impact on temperature and velocity forecasts near the Ka'iwi Channel.

Table of Contents

Acknowledgements	ii
Abstract	iii
Table of Contents	iv
List of Tables	v
List of Figures	vi
Chapter 1: Introduction	1
Chapter 2: Background	3
2.1: ROMS	3
2.2: Sensors	5
2.3: Physical Setting and Background Circulation	14
2.4: Model Consistency	16
2.5: HIOG and Mamala Bay Circulation	24
Chapter 3: Methods	42
3.1: Twin Experiment	42
3.2: 4DVar	43
3.3: Observing System Simulation Experiments	45
3.4: Experiment Setup	48
3.5: Synthetic Observations	
3.6: OSSE Test Cases	
Chapter 4: Results/Discussion	53
4.1: Full Grid	53
4.2: Mamala Bay	56
4.3: OTEC at plume depth	58
4.4: Analysis of Results	59

Chapter 5: Conclusions	75
References	77

List of Tables

- 2.1 Honolulu Tide Gauge - ROMS Root Mean Square Error
- 3.1 Errors of Representativeness
- 3.2 Observing System Sampling Coverage

List of Figures

- 2.1 HIOG Study Site with regional bathymetry from the Hawai'i Mapping Research Group. Regions of interest are highlighted and labeled.
- 2.2 Canonical Circulation from Lumpkin(1998)
- 2.3 Mean Annual Satellite SST Comparison between HIIG and AVHRR Satellite data
- 2.4 Mean Winter and Summer SST Comparison between HIOG and AVHRR Satellite data
- 2.5 Temperature and Salinity RMS between 2008 Seaglider data run within HIOG model and HIOG model data
- 2.6 Differences of M_2 Tidal Phase and Amplitude Radial Velocities between HFR observations and HIOG model data
- 2.7 Vorticity and velocity comparisons computed from HF Radial velocities and HIOG data
- 2.8 Barotropic Tidal Ellipses along south shore of Oah'u
- 2.9 Ka'iwi Channel Mean Seasonal Velocity (m/s) Transect between Kokohead and Molokai
- 2.10 Barotropic Seasonal Mean Velocity (m/s) Upper 70m
- 2.11 HIIG Ka'iwi Channel Transect Mean Annual Velocity (m/s)
- 2.12 Mean Seasonal Surface Baroclinic Instabilities
- 2.13 Mean Seasonal Upper 70m Baroclinic Instabilities
- 2.14 Vorticity vs. Strain Across HIOG
- 2.15 Transport timeseries with tidal residual overlaid
- 2.16 Density Hoffmueller Plot at OTEC site
- 2.17 Annual Velocity at OTEC Plume Depth (215m)
- 3.1 Sensor Coverage Areas. Radar shown in green, glider in red, mooring in blue, sea surface height satellites in pink, and sea surface temperature satellites cover entire grid.
- 4.1 Temporal Median HIOG Upper 70m Forecast Temperature (K); RMS on top, Correlation on bottom
- 4.2 Spatial HIOG Upper 70m Temperature (K) Forecast RMS Sensor Impact
- 4.3 Spatial HIOG Upper 70m Temperature (K) Forecast Correlation Sensor Impact
- 4.4 Temporal Median; HIOG Upper 70m Forecast Velocity (m/s); RMS on top, Correlation on bottom
- 4.5 Spatial HIOG Upper 70m Velocity (m/s) Forecast RMS Sensor Impact
- 4.6 Spatial HIOG Upper 70m Velocity (m/s) Forecast Correlation Sensor Impact
- 4.7 Surface Velocity Energy Density (m^2/s^2); Overlaid with best case on top, Error bars included on bottom

- 4.8 Sensor Impact on Growth rate of Upper 70m Baroclinic Instability (s^{-1})
- 4.9 Sensor Impact on Barotropic Okubo-Weiss Parameter ($S^2 - \omega^2$)
- 4.10 Temporal Median; Mamala Bay (Upper 70m) Forecast Temperature (K); RMS on top, Correlation on bottom
- 4.11 Spatial Mamala Bay (Upper 70m) Temperature (K) Forecast RMS Sensor Impact
- 4.12 Temporal Median; Mamala bay (Upper 70m) Forecast Velocity (m/s); RMS on top, Correlation on bottom
- 4.13 Spatial Mamala Bay (Upper 70m) Velocity (m/s) Forecast RMS Sensor Impact
- 4.14 Temporal Median; Mamala Bay (70-150m) Forecast Temperature (K); RMS on top, Correlation on bottom
- 4.15 Spatial Mamala Bay (70-150m) Temperature (K) Forecast RMS Sensor Impact
- 4.16 Temporal Median; Mamala bay (70-150m) Forecast Velocity (m/s); RMS on top, Correlation on bottom
- 4.17 Spatial Mamala Bay (70-150m) Velocity (m/s) Forecast RMS Sensor Impact
- 4.18 Temporal Median; OTEC Plume Depth (215m) Forecast Density (kg/m^3); RMS on top, Correlation on bottom
- 4.19 Spatial OTEC Plume Depth (215m) Density (kg/m^3) Forecast RMS Sensor Impact
- 4.20 Temporal Median; OTEC Plume Depth (215m) Forecast Velocity (m/s); RMS on top, Correlation on bottom
- 4.21 Spatial OTEC Plume Depth (215m) Velocity (m/s) Forecast RMS Sensor Impact

Chapter 1

Introduction

Ocean forecasting requires a model constrained by observations and, as funding for those observations becomes limited, it is important to identify which data contribute to the most accurate forecasts. Unlike numerical weather prediction (NWP), extensive daily profiling is not available within the ocean and understanding which observations optimize forecasting is essential for effective policy and model development.

Regional ocean models provide numeric simulations of ocean dynamics. They can be used to investigate small-scale variability that is not represented by global ocean models and produce more accurate local ocean forecasts. The research contained herein uses a regional ocean model, covering the south shore of Oah'u with a twin experiment to conduct an observing system simulation experiment (OSSE). While analysis of the data produced by multiple sensors provides important insight into local ocean dynamics, certain observations prove more useful to forecast relevant ocean processes. These experiments assess various ocean observing systems to determine their impact on model forecasts. These particular study sites are distinctly challenging for models because of the complex tides, including internal tides, rapidly varying bathymetry, mesoscale energy impinging on a shallow coast and overall dynamic structure.

Mamala Bay and a potential ocean thermal energy conversion (OTEC) plant site off Barbers Point were chosen to evaluate the impact of various observing sensors on the regional model forecasts in addition to analysis of the forecast across the entire model space. Mamala Bay was selected as it is a focus area for the Hawai'i Ocean

Observing System (HiOOS). HiOOS is a component of the Pacific Islands Ocean Observing System and is tasked with support of the U.S. integrated ocean observing system. The OTEC site was selected as it is the proposed site of a pilot program for a moored OTEC facility designed to produce 100MWe.

The rest of this manuscript is organized as follows. Chapter 2 provides background information for the OSSEs, details of the regional ocean model used in this study, and a comparison of model output to *in situ* sensors. Additionally, the selection and locations of the sensors are explained, as well as an analysis of circulation around Oah'u with specific focus on the experimental areas of interest. Chapter 3 is a discussion of the methods used to set up the twin experiment and to run the OSSE. The results and a discussion of those findings are presented in Chapter 4. Finally, conclusions are presented in Chapter 5.

Chapter 2

Background

2.1 ROMS

Regional ocean models are used to study ocean circulation and climate. Most are generated using primitive equations and bounded on all sides by land or water.

Boundary conditions are used to incorporate solutions from larger models.

Atmospheric forcing provides surface boundary conditions, and bottom boundary conditions are derived to represent bottom forcing from interaction with Earth (rock, sediment, etc...). The primitive equations stem from geophysical simplifications of the Navier-Stokes equations for fluid motion and are a set of non-linear equations used to approximate atmospheric and oceanic flows. The equations of motion of a fluid may be explained by three primary concepts. The continuity equation represents the conservation of mass,

$$\frac{\partial \rho}{\partial t} + \nabla \cdot (\rho \mathbf{v}) = 0$$

where ρ represents density and ν kinematic viscosity. The momentum equation conserves momentum and describes hydrodynamical flow on the surface of a sphere.

It is given by:

$$\frac{D\vec{v}}{Dt} = -\frac{\nabla p}{\rho} + \nu \nabla^2 \vec{v} + \vec{F},$$

where \vec{F} represents the effects of body forces such as tides, $\nu \nabla^2 \vec{v}$ is the friction term and p is a measure of pressure. The thermodynamic equation is given by:

$$\frac{DI}{Dt} + \frac{p}{\rho} \nabla \cdot \mathbf{v} = \dot{Q},$$

where \dot{Q} represents diabatic sources such as heating and diffusion (Vallis, 2006).

The thermodynamic equation conserves heat and salt. The primitive equations are simplified using the following approximations:

- I. The hydrostatic approximation, $\frac{\partial p}{\partial z} = -\rho g$. This can be used assuming the horizontal scale is large compared to the vertical scale, such that the fluid can be considered incompressible.
- II. The shallow-fluid approximation assumes fluid is homogenous.
- III. The traditional approximation that the horizontal Coriolis terms in the momentum equations involving the vertical velocity are neglected. (Vallis 2006)

The model used for this study is the Regional Ocean Modeling System (ROMS); a free-surface, hydrostatic, primitive equation, ocean model with a terrain-following vertical coordinate system and a mode splitting technique (between barotropic and baroclinic modes) for time stepping (Shchepetkin and McWilliams 2005). The mode splitting between barotropic and baroclinic modes facilitates effective time integration. While the model can be tailored to capture coastal-to basin-scale circulation, the terrain-following vertical coordinates are useful for more regional applications, such as high resolution coastal zones, as seen in this study. However, it is important to minimize errors in the horizontal pressure gradient (Shchepetkin and McWilliams, 2005). Consequently, the vertical coordinate system requires smoothing of bathymetry, which can negatively influence coastal zones by dampening bathymetric slopes.

This ROMS was configured for the Hawai'i Ocean Observing System (HIOOS). It is a nested grid model, in which smaller-scale, higher-resolution grids are placed within the larger regional model. These are used to provide more detail within the region of coastal and small scale dynamics. The largest and outermost grid for HIOOS is the Hawaiian Islands Grid (HIIG). The four boundary conditions are provided by the Navy Coastal Ocean Model (NCOM) using daily global forecasting with $1/8^\circ$ resolution. HIIG has 4km horizontal resolution and 30 vertical sigma layers. This study is conducted in one of the higher-resolution child grids nested within HIIG, the

Hawaiian Islands Oah'u Grid(HIOG), Figure 2.1. It has 1.1km resolution and 30 vertical sigma layers. Boundary conditions are imposed by the surrounding HIIG conditions. Atmospheric forcing for HIIG is imposed by MM5, the fifth generation Pennsylvania State University and National Center for Atmospheric Research (NCAR) mesoscale model. MM5 is a limited-area, nonhydrostatic, terrain-following sigma-coordinate model designed to predict mesoscale-atmospheric circulation. The MM5 fields are specified every three hours to capture the diurnal heat flux cycle. The atmospheric fields that force the ocean model include surface air temperature, rainfall rate, surface air pressure, surface winds at 10m, net longwave radiation flux, solar shortwave radiation flux, and surface air relative humidity.

2.2 Sensors

Observational data provide measurements of various ocean properties at a specific space and time location. These data can be assimilated in models to improve the measurement of the ocean state. For this study, satellites, high frequency radio, a buoyancy driven autonomous glider, and an *in situ* mooring are evaluated. The following is a discussion of each observing system including history, capabilities, strengths and limitations of each sensor. For this study, synthetic observations were used to represent observing systems since some were not available in the study area. The HF radar station at Barbers Point was not available at the start of this experiment although it is now operational. Other sensors, the seaglider and mooring, were not available for the experiment.

2.2.1 Satellites

Satellite data present enormous benefits to the oceanography community. Through in-depth studies of electromagnetic radiation and the resulting interaction with matter, scatter and emission from rough surfaces were studied, and it became apparent that satellites could be used to study sea surface (Stewart, 1985). As oceanographers

became more involved in the use of space as a medium to study the ocean on a global-scale, more instruments were designed to specifically examine the oceans. Stewart (1985) offered three reasons for studying the ocean from space: to obtain a global picture of the oceans in order to study basin-wide phenomena; to observe regions not easily studied by ship, for example, the Southern Ocean around Antarctica in winter; and to make measurements that are either impossible or difficult by ordinary means, such as observing oceanic rainfall or the distribution of small waves on the sea surface. This global approach, which originated with meteorologists, allows for the inclusion of ocean impacts on climate variability studies. For this study, two types of satellites were considered; sea surface height and sea surface temperature.

2.2.1.1 Sea Surface Height (SSH) Satellites

Three primary SSH Satellites are in orbit today: Jason 1, Jason 2, and Envisat. These satellites measure dynamic sea surface height.

Jason 1 was developed as a joint program with NASA and Centre National d'Études Spatiales (CNES) in France. It is a successor to the TOPEX/Poseidon mission designed to continue to measure ocean surface topography. Over the long term, this data is used to assess global sea level changes, but it is also of a fine enough scale to detect hills and valleys in the sea surface to determine ocean current flow and global scale circulation. Launched on December 7, 2001, Jason 1 began collecting its first cycle of data on Jan 15, 2002. Jason 2 also known as OSTM (Ocean Surface Topography Mission), is a follow-up to the TOPEX and Jason 1 missions. Jason 2 was launched on June 20, 2008, and began collecting data on July 12, 2008. Jason 1 and Jason 2 are designed to orbit the Earth one half cycle apart to provide better temporal resolution, with the Jason 1 ground track falling between Jason 2's track for an interwoven and improved spatial coverage. Both Jason satellites have similar

orbital specifications and sampling resolutions. The Jason satellites maximum orbit is 66.15° with an orbit cycle of 9.9156 days. They travel at 5.8km/s over ground with a control band of ± 1 km on a direct path. Both Jason 1 and 2 have an orbital accuracy of ~ 2.5 cm. They carry a Poseidon 2 nadir pointing radar altimeter that measures sea level accuracy to better than 4.2cm. The sensors sample at 100Hz, but the samples are filtered to 10Hz and 1Hz (JPL, 2006).

Envisat-1 is an environmental satellite developed by the European Space Agency (ESA) as a follow up to the ESA Remote Sensing satellites, ERS-1 and ERS-2. The intention is for Envisat-1 to continue the ERS measurements for long-term data sets. This will continue the missions of climatological and environmental research with added capability. It was launched in March, 2002 and uses the Radar Altimeter 2. This is an improvement from the Radar Altimeter 1 on the ERS satellites; the satellite can now measure sea surface height to better than 4.5 cm. Envisat also carries an Advanced Synthetic Aperture Radiometer (ASAR) and Microwave Radiometer (MWR). ASAR is an improvement from the SAR instruments on the ERS missions. Both ASAR and MWR can be used with the altimeter to measure significant wave height, wind speed, and sea state. They both operate using the principles of radar backscatter measurements to determine surface roughness. Envisat has a sun synchronous polar orbit, with 98.55° inclination. The orbit has a maximum deviation of ± 1 km from ground track and an orbital period of 101 min with a repeat cycle every 35 days.

The major benefit of the SSH satellites is the complete global coverage they offer. They allow for identification of trends and surface height shifts across the ocean surface. As several countries use the easily accessible satellite data and share the costs of maintenance, the individual burden is also greatly reduced. SSH is generally used to study the surface ocean, but it can detect subsurface properties through

baroclinic and barotropic expressions. Despite all the benefits, however, weaknesses of using satellites to collect oceanographic data must be considered. Satellites are operating from space, so, while instruments have broad spatial coverage, some interpolation is required to define spatial resolution. If the size of a region under investigation is too small, requisite interpolation may be too significant to detect regional phenomena. Additionally, Jason 1 and 2 can not be used within 40km of land without special processing, which may introduce error. Lastly, while temporal resolution is sufficient on a climatological time scale, phenomena on a shorter time scale will not be evident.

2.2.1.2 Sea Surface Temperature (SST) Satellites

There are four SST satellites in primary operation right now. The National Oceanic Atmospheric Administration (NOAA), in cooperation with the European Organization for the Exploitation of Meteorological Satellites (EUMETSAT), is using NOAA 19 and METOP-A as their primary pm/am satellites respectively, while NASA also has Aqua and Terra in orbit. NOAA 19 and METOP-A are the most recently launched satellites as part of NASA's Polar Operational Environmental Satellite (NPOESS) program. They are the latest in a series of satellites that have been operating since 1978 with many successful missions. There are always two satellites in orbit as a morning and afternoon satellite to ensure full global coverage at least once every 12 hours. First and foremost, SST satellites are providing critical imagery for weather forecasters as they have such frequent global imagery to input in forecast models and to monitor weather system development. Missions that SST satellites are used for include: providing critical data for long term studies including climate research, global sea surface temperature measurements, measurements of temperature and humidity of the atmosphere, ocean dynamics research, volcanic eruption monitoring, forest fire detection, and global vegetation analysis. NOAA 19 and METOP A operate with identical orbital parameters (12-hours apart) to maintain

continuity. They are polar orbiting satellites with an inclination of 98.7° . They have a 101 minute orbit and complete 14 cycles per day. They operate in a lower orbit than some of the other satellites, from as close as 833km (NOAA 19) and 817km (METOP-A.) Unlike the SSH satellites, they use a swath based sensor which is 2399km wide. However, each instrument has different requirements, so swath size varies with each instrument. The instrument providing critical information for ocean modeling is the Advanced Very High Resolution Radiometer (AVHRR/3) with a spatial resolution of 1.1km at nadir that scans the earth from $\pm 55.4^\circ$.

Aqua and Terra are two satellites operating much like the NOAA 19/METOP-A satellites providing am/pm global coverage. They have a similar mission to provide data to help improve our understanding of global dynamics both over land and water and in the lower atmosphere. Critical sensors in earth system models and global climate change predictions, Aqua and Terra also have varied orbits. Terra proceeds north to south across the equator in the morning and Aqua passes south to north across the equator in the afternoon. They cover the entire earth's surface in one to two days and the Moderate Resolution Imaging Spectroradiometer (MODIS) instrument acquires radiometry data in 36 spectral bands, ranging in wavelength from $0.4 \mu\text{m}$ to $14.4 \mu\text{m}$. Two bands have a surface resolution of 250m at nadir, five bands have a surface resolution of 500m and the remaining 29 bands are resolved at 1km. Per MODIS technical specifications documentation, MODIS uses a $\pm 55^\circ$ scanning pattern at 705km and achieves a 2330km swath to provide full global coverage.

SST satellites have most of the same benefits and weaknesses as the SSH satellites. Some important differences are that SST satellites only sample the surface and are limited by cloud coverage. SSH can offer more explanation of the density structure than the SST satellite capabilities allow. However the temporal resolution is better for SST such that these satellites can track weather systems and changes on a smaller

time scale. Most importantly, these satellites are used in weather forecasting. Also SST satellites use a passive sensor which detects energy emitted from the earth, while SSH satellites use an active technique in which they emit set wavelengths of energy and then track the strength of the return of those emissions. SST satellites provide an important snapshot of temperatures across the entire surface ocean, while SSH satellites provide profiles when it flies directly over the area of interest.

2.2.2: High Frequency Radio (HFR)

High Frequency (HF) Radio detection and ranging (Radar) is used to observe ocean surface currents. HF radar uses high frequency signals to track significant wave height and surface current direction. It uses the processing of second order radar return to compute the 2D frequency direction spectrum at each grid point of coverage. In 1977, Coastal Ocean Dynamics Application Radar (CODAR) was the first HF radar developed to use electromagnetic wave backscatter from a rough sea surface to measure surface currents (Barrick 1977, Essen et al. 2000). CODAR uses a continuous wave (CW) pulsed modulation scheme for range resolution and a square arrangement of 4 receive antennas for azimuthal resolution (Gurgel, 2001). In 1983, E.D.R. Shearman presented results from his PISCES HF radar system in which he used Frequency Modulated Interrupted Continuous Wave (FMICW) modulation for range resolution and a large linear array of receive antennas which seemed to extend the range of wave measurements and in turn currents. The University of Hamburg developed the Wellen Radar (WERA) in 1996 using FMCW (Gurgel, 2001). WERA is the HF radar currently used in wave measurement and surface current experiments off the south shore of Oah'u, operated by Dr. Pierre Flament, University of Hawai'i at Manoa, primary investigator for the HIOOS HF Radar.

HF Radar operate by using shore based transmit antennas to send a low power HF radio signal across the ocean. This signal reflects off ocean waves and receive

antennas capture the electromagnetic (EM) backscatter from those reflections. Wave speeds are generally predictable, so by analyzing the doppler shift of EM return pattern, wind direction and wave spectrum can be determined. EM waves reflect off (ocean) waves with exactly half the radio wavelength (Essen, 1999). Receive antennas capture return frequency from reflected EM waves and the difference can be used to determine a doppler shift. An individual radar can only be used to determine radial currents, velocity of the waves toward or away from that radar station. These can be derived exactly from the gravity wave dispersion relationship. However with two HF Radio sites, operating some distance apart, at an angle as close to normal as possible, vector currents can be inferred from the radial measurements (Essen, 1999).

HF Radar provides good temporal and spatial resolution on the surface of the ocean. It is also not subject to a harsh marine environment since it is located on land. It does not, however, provide velocity structure below the surface. Data can be inferred given wind direction and wave spectrum at the surface, but it is primarily a surface ocean asset for determining surface velocities. Other limitations include the data being processing intensive and requiring significant coastal real estate and permitting.

2.2.3: Underwater Gliders

Underwater gliders are a source for subsurface ocean observations including temperature, salinity, optics, biological measures, acoustics and others. There are three primary underwater gliders in operation today; the Spray, the Slocum and the Seaglider. For this study, we will use the Seaglider, which is in operation by Dr. Glenn Carter.

Seaglider is an autonomous underwater vehicle that profiles vertically and horizontally by controlling buoyancy with modest energy requirements. Gliders use buoyancy to generate vertical motion and lift produced by its wings to propel itself

forward. They travel at low speeds, which keeps their drag very low and in turn greatly extends their longevity on patrols. Missions can last several months across entire ocean basins (Rudnick, et al., 2004, Eriksen et al, 2001). Gliders can measure temperature, salinity, and other parameters when outfitted with appropriate instrumentation, using a saw toothed vertical track profile.

The US government began funding research and development of underwater ocean gliders in the late 1990s. Seaglider was originally designed and developed by the University of Washington(UW) Applied Physics Laboratory in conjunction with the UW School of Oceanography. It went through many field trials in Puget Sound, which proved successful and they are now in use by many institutions around the world. With a body length of 1.4m, a wingspan of 1m, the glider has a maximum depth of 1000m and a maximum range of 4600km. Assuming 1km depth for dives, it can complete 650 dives with a typical speed of 0.24m/s (Seaglider Specifications provided by University of Washington, SoO and APL, copyright 2005, <http://seaglider.washington.edu/>)

Ocean gliders provide many advantages: they are relatively inexpensive with respect to equipment costs, manpower costs and outside assistance such as ship deployments; they can be deployed and recovered with a minimum of two persons and a small recovery vessel. A glider can also operate as a “virtual mooring,” by being programmed to conduct repeat profiles at the same location. If the currents are not stronger than the glider speed, it can maintain station as well as a moored buoy, O(1km)(Weller, et al., 1990). It can also be deployed to go to a station and conduct repeat profiles continuously. While they do not necessarily resolve higher frequency phenomena, they have less material and labor requirements to maintain them, and could potentially serve as an excellent substitute to a natural mooring (Rudnick et al, 2004). Seagliders can also be used as a “virtual,” vessel towed sensor as they can be

provided a course to travel using their saw-toothed travel pattern. They can cover significant area (entire ocean basins) without requiring a ship and its crew on station to facilitate deployment.

One of the disadvantages of the Seaglider program is that since they are autonomous they may be lost. When using the glider, as a “virtual mooring,” it will not have quite the same spatial resolution as it will be somewhat subject to currents, but it is able to maintain station much like a mooring does with a swing radius. It uses dead reckoning to adjust its course every time it surfaces and confirms its location, but it will have more variability than an actual mooring. Also as the glider will be moving vertically continuously, it will not be taking continuous readings at any given depth. Overall, Seagliders provide an excellent underwater autonomous observing sensor for ocean research.

2.2.4 *In Situ* Mooring

In situ moorings are a source of temporal and vertical spatial ocean observations. *In situ* moorings can be configured with various sensors stationed at assorted depths along the mooring. They are designed to be on station for an extended period of time gathering data to conduct time series analysis of the ocean. Sensors can range from biological to chemical to physical. For purposes of ocean modeling, possibly the most useful sensors are the conductivity, temperature and depth (CTD) and acoustic dopplar current profiler (ADCP) sensors. Moorings are very versatile and can be designed to meet the needs of most any single point research since they can stay on station for extended periods of time with limited human involvement. However, when they are recovered, instruments require significant maintenance and upkeep. Sensors can be placed at most any depth to capture temperature, salinity, currents, biological activity and more. The temporal resolution is limited by the memory or data delivery capabilities of the instruments on the mooring. Temperature and

salinity are captured using a conductivity, temperature, depth or pressure (CTD) sensors. Currents are measured using an Acoustic Doppler Current Profiler (ADCP). There are many other sensors that can be placed on a mooring for data collection as well.

One of the major disadvantages to a mooring is the minimal horizontal spatial resolution. The mooring only gathers data at its exact location and within the swing radius of the mooring. While it would be ideal to have moorings all over the ocean, that is not logistically feasible. Consequently, moorings are mainly able to give a snapshot of one spot in the ocean. Additionally, deployment and recovery of the mooring can be costly and often requires a larger vessel and several personnel depending on the size of the mooring. The time series data still provides an essential indicator of ocean conditions. The longer the mooring can be kept on station, the more useful it can be for monitoring longer range periodic ocean trends.

2.3 Physical Setting and Background Circulation

The Hawaiian archipelago is an isolated island chain located in the North Pacific subtropical gyre between 19°N and 22°N. The southern boundary of the North Pacific gyre is the North Equatorial Current (NEC), driven by the NE trade winds. The North Pacific high pressure system produces these dominant winds which occur almost year round. Tides around the islands are of a mixed type with a mean amplitude range of 0.5 to 1m. Due to the islands' distinctive isolation in the middle of the Pacific plate, their steep bathymetry combined with tidal flow angle across this bathymetry produce many internal tide generation sites, causing significant mixing in the area.

The mountainous Hawaiian islands provide an important wind blocking effect, that when coupled with ocean-atmosphere dynamics have important large-scale

circulation influence (Chevanne, et al. 2002). Oah'u is subject to prevailing east to northeast trade winds. These winds produce trade wind waves, which occur about 75% of the time and have a mean significant wave height of 4.8ft and a wave period of 8.6s. Kona winds and waves occur 10% of the time. They are generated by local storms with a mean significant wave height of 3.5ft and a period of 6.2s (Wang, Gerritsen, 1995). As the trade winds are forced between the islands, wind stress curl anomalies occur. On the north sides of the islands cyclonic eddies are formed and on the south sides, anti-cyclonic eddies are created, which produce upwelling and divergence on the northern sides of the islands and downwelling and convergence on the southern sides, generating mixing (Barton 2001, Chavanne 2002). Additionally, these wind stress patterns influence the currents west of Hawai'i.

The canonical circulation is shown in Figure 2.2 taken from Lumpkin (1998). When the NEC reaches Hawai'i, the largest island furthest east on the chain, it splits. The NEC travels south around Hawai'i, and continues south and west. The northern arm flows around the island, known as the North Hawaiian Ridge Current (NHRC), and continues NW on the northern side of the chain (Qiu et al., 1997). The Hawaiian Lee Counter Current (HLCC) flows from west to east just north of the NEC. It is driven by wind stress patterns, toward the Big Island (Lumpkin, 1998). Eddies are often formed in the lee of the Big Island, most likely due to the wind stress curl (Calil, et al). Lumpkin (1998) also showed an island wake exists west of the islands which includes two elongated, counter-rotating gyres that extend 1000km west of Hawai'i, separated by the HLCC. Xie, et al. (2001) using satellite data, found evidence the wake may extend as much as 3000km west of Hawai'i. The last major island current influence is the Hawaiian Lee current (HLC), which runs west-northwest along the leeward coasts and through channels between the islands. The HLC returns some of the water brought east by the HLCC, back to the west (Lumpkin, 1998).

A vertical transect of the larger HIIG grid at longitude 157.46W cutting through the Ka'iwi Channel is shown in Figure 2.11. This transect shows the six year mean velocity across the transect. From left to right, the NEC current can be distinguished by the deep dark blue which reaches just below 100m at its greatest magnitude. However, its impact can be detected to over 1000m. The eastward flowing HLCC is shown by the strong Eastward jet, extending to approximately 300m depth. The HLC is very weak and shown as the western current and the exchange across the Ka'iwi channel south of Oah'u is shown by the two red currents on either side of the seamount. The NHRC is given by the smaller magnitude westward current, reaching approximately 200m.

Below the surface, the bottom topography is dominated by seamounts from the island chain. These are an important circulation parameter as they provide a guide for subsurface current flow. Circulation is bounded by land masses, so flow will adjust to move around them (Chevanne, et al. 2002). Most importantly, the steep bathymetry of the islands facilitates the development of internal tides.

Internal tides are generated through a barotropic-to-baroclinic conversion. They are generated in stratified waters when barotropic tides interact with seamounts or other abrupt topography. Their strength and influence is also dominated by the angle in which the barotropic tides impact the bottom topography. The closer the angle is to normal, the stronger the internal tide generated (Garrett and Kuntze 2007, Carter et al. 2006). The combination of steep topography and direction of the M2 barotropic tidal propagation makes the Hawaiian Ridge the largest generator of M2 internal tides by area in the world's oceans. Many aspects of these baroclinic tides and their effect on turbulent mixing have been studied recently, for example Holloway and Merrifield (1999), Carter et al. (2006), Carter et al. (2008), and Chavanne et al. (2010).

This is a complex, dynamical region that is enhanced when we focus on the southern side of the island of Oah'u. Complex bathymetry makes the region an internal wave generation site, strong winds drive small-scale and mesoscale energy that impacts the coast and all combine to make the HIOG region exceptionally challenging to model and predict.

2.4: Model Consistency

Because the region is so complex, we must determine if the modeled flow is consistent with observed characteristics. We conducted a run of the HIIG and HIOG models without assimilation of any data, forced by global NCOM at the boundaries and MM5 at the surface for the period 2004-2009. We compare the 6 year model run to the Honolulu Tide Gauge (HTG), satellite SST data, and glider data from a 2008 Seaglider mission flown between Oah'u and Penguin Bank. Additionally, we include an analysis between HF Radar data from Kokohead from summer 2009 to spring of 2010 and ROMS, performed by Cass (2010). The techniques and results are discussed below.

2.4.1 Honolulu Tide Gauge (HTG)

HTG has been collecting tide gauge data since 1873 (Colossi and Munk, 2006) but reliable data dates back to 1905. Located inside of Honolulu Harbor, HTG is not directly represented in the HIOG model. The nearest representative grid point that could be directly compared is 3.04km away. Data sampled at 1hr intervals from station files were compared for 2008. Tidal amplitude and phase were determined for each data set using the primary constituents M_2 , S_2 , K_1 , O_1 , K_2 , N_2 , and P_1 . From Cummins and Oey (1997), the amplitudes and phases between the tide gauge and model can be used to quantitatively compare tides with an absolute root mean square error (RMSE) using,

$$E = \sqrt{\frac{1}{2}(A_o^2 + A_m^2) - A_o A_m \cos(G_o - G_m)}$$

where A represents amplitude, G the phase, subscript 'o' represents observed values (HTG) and 'm,' the modeled. The RMSE over the 6 years was calculated for each of the major constituents listed above and is presented in table 2.1. M_2 has the greatest amplitude and drives much of the energy, yet it also has an error of 2.15cm, which is only 14% of the signal. K_1 has the next greatest amplitude and also drives a lot of the energy. It has an error of 1.19cm which makes up only 8% of its signal. The last of the top three constituents is S_2 which has an error of 0.29cm, which makes up 6% of its signal. While providing less energy than M_2 and K_2 , it has a very low error.

2.4.2 SST

Seasonal mean satellite SST data and ROMS were also compared for consistency. Pathfinder AVHRR data from the NASA Physical Oceanography Data Active Archive Center (PO.DAAC) over the modeled period was used. This data has a 4km resolution, but is not spatially complete due to clouds, etc. Data was compared in two stages. Initially, data from across the larger HIIG was compared. Data from HIOG was overlaid on top of the HIIG to evaluate consistency between the parent and child grid in addition to consistency between the model and the observational data. As shown in Figure 2.3, the modeled field is much smoother than the observed SST; however, the primary signals are similar in both. Between the islands (particularly the Big Island and Maui), cooler water entrains due to upwelling and increased winds. This is captured by the model but it is not as strong as observed. Overall, the model exhibits a warm bias of 0.22K owing to the depth of the first layer, which is not directly comparable to SST observed by satellite. Observational data showed consistent trends to the model, both the parent and child grid, although the model has coarser resolution. To more thoroughly compare the observations directly to HIOG, a seasonal comparison was used (Figure 2.4). The model contains a 0.25° warm bias in the winter and a 0.36° warm bias in the summer. These errors can in part be attributed to differences in how the temperatures are collected. ROMS sigma level

values at the surface grid level are set at different depths based on the depth of the water. The temperature value at the surface grid cell could be as close as 50cm from the surface, to over 2m deep, therefore they may show much greater variability and also may not capture the same temperature the satellite is sampling. SST values from satellites are a regression of skin surface radiance to a 1m “bulk” temperature, but are truly representative of only the surface boundary layer. Most likely, the warm bias can be attributed to the thicker surface layer of the model, which does not capture the full variability of the diurnal SST cycle. In addition to the diurnal heat flux, there can be a warming in the wind wake of islands as discussed by Xie et al.(2001) and Chavanne et al.(2002). Xie et al. discusses the strength and influence of the wind wake that occurs behind the islands. Chavanne et al. suggests Ekman pumping in the lee of the islands is warming surface temperatures in the lee. As strong winds are traveling between the islands, wind speed variations causes divergent and convergent surface currents, which in turn depress or lift the thermocline. The differences between the model data and satellites are most likely attributed to these phenomena. However, Figures 2.3 and 2.4 still show generally positive agreement overall between seasonal satellite SSTs and ROMS, even with the surface heat flux variability.

2.4.3 Glider

A Seaglider, operated by Dr. Glenn Carter as part of HiOOS program collected data off of the South Shore of Oah'u from April to August 2008. As gliders capture the internal tides, but sample them moving in space and time, it is difficult to compare them to model data. These internal waves are at different phasing in the model, and a heaving isopycnal can cause the glider to sample water with very different properties than that of the model at the same time. Additionally, if the glider is traveling near the boundary of the thermocline, it can also sample water with very different properties than the model at the same place in time and space. In an attempt to mitigate these effects, glider and model data from the sampling period were binned by

depth and the RMS difference between the model and observed bins for temperature and salinity were computed at each depth layer. The data were binned in ~50m increments to ensure similar quantities of data were used at each depth. Figure 2.5 shows the RMS for temperature and salinity between the Seaglider and model. The temperature and salinity both have peaks in RMS at the 150m depth, which corresponds to the approximate mean thermocline depth suggesting that internal wave displacement at this depth results in large differences between the model and observations. Away from the main internal wave pathways, we find much closer comparison to the glider with RMS less than 1K and 0.2 psu.

2.4.4 HF Radar

M_2 has been shown to be the most dominant tidal constituent around the Hawaiian Islands (Eich et al, 2004, Carter, et al., 2008). Cass (2010) performed a thorough comparison of surface radial tidal currents from a HF radar located on Kokohead with several different models, including HIOG to examine the variability in the models and the harmonic analysis of HF radar. Tidal variance is compared using tidal ellipses with inclination, phase, major and minor axes in which inclination represents the orientation of the axes and phase is the time lag from Greenwich. To allow a uniform comparison in the study, HF Radar data was regridded to match horizontal spacing, interpolated across small time gaps, filtered to reduce low frequency impacts and model outputs were projected into the radial reference frame to ensure no phase ambiguity. Cass found HIOG data showed positive phase agreement with the radar along the southeast shore of Oah'u and near Penguin Bank, a slight lag west of Pearl Harbor and a lead south and west of Barber's Point. ROMS underestimates tidal amplitudes near shallow features, probably because the bathymetry at 1.1km resolution can not reproduce the true features, but accurately reproduces features in the Ka'iwi Channel. Overall, there was good agreement between the model and

observed HF surface currents (Cass, 2010). Figures of the differences in phase and amplitude between ROMS and the observations are shown in Figure 2.6.

In addition to the M_2 tidal variance, Cass (2010) also looked at the vorticity computed using measured radial currents. For this comparison, vorticity was calculated the same way using model data, for the area across the HF coverage. The results are seen in Figure 2.7. While the model data shows lower vorticity magnitudes, the model has consistent trends with the observed data. Positive vorticities are seen on the eastern side of headlands, while negative vorticities are seen on the western side of headlands along the south coast of Oah'u.

2.5 HIOG and Mamala Bay Circulation

We use the 2004-2009 model run to investigate the circulation on the south side of Oah'u. The seasonal and annual trends are analyzed as well as the influences of tidal forcing, current velocities, and instabilities on local circulation. In addition to the steep bathymetry of Oah'u and Moloka'i, Penguin Bank extends southwest from Molokai along the south east side of Oah'u, providing an exceptionally shallow Bank surrounded by much greater depths. The influence of Penguin Bank will be highlighted throughout this discussion.

Tides in Oah'u are of mixed type. The tidal range between mean lower low water and mean higher high water is 0.58m with a maximum tidal range of 1.3m (Wang, Gerritsen, 1995). Tidal forcing plays a dominant role in the coastal dynamics along the south shore of Oah'u. Bathymetry drives currents primarily alongshore and almost directly through the center of the Ka'iwi Channel. Figure 2.8 displays several tidal ellipses from across the entire grid representing the major tidal flow. The tidal ellipses' semi-major and semi-minor axes were calculated using radii from the tidal analysis of depth averaged currents for one year of data. The tidal analysis used 7 major tidal constituents M_2 , S_2 , K_1 , O_1 , K_2 , N_2 , and P_1 with the matlab function T-tide

(Pawlowicz et al. 2002). The ellipses generally trend alongshore or along bathymetry contours. The ellipses are much larger when the current flow is much greater as seen across the shallower water of Penguin Bank and across the Kaena Ridge on the west side of Oah'u. The longer asymmetrical ellipses suggest flow is primarily in one direction, along the major axis of the ellipse. This is seen with the ellipses going through the Ka'iwi Channel. The tidal flow is almost directly through the channel.

Hawai'i is located in the tropical latitudes, so while it does not experience seasonal shifting as extreme as more poleward locations, seasonal trends are evident particularly in the upper 70m of the water column. The HLCC, as discussed above, flows eastward toward Hawai'i and transports a large amount of heat. As it arrives in the lee of Hawai'i, it splits and part of its flow becomes the HLC which returns some of that heat to the west, traveling north between some of the islands including Oah'u and Molokai (Lumpkin 1998). This drives the surface currents in the Ka'iwi Channel north and east through the channel. Figure 2.9 shows a vertical transect of current through the channel which ran between Oah'u and Molokai from 21.115N/157.31W and 21.285N/157.655W. It shows below the surface a counter-current exists. The depth of this counter-current varies seasonally. The thermocline deepens with colder temperatures experienced in the winter, but a lag exists in oceanic temperatures such that the deepest thermocline is found in the spring. This pushes the counter-current deeper during the spring, but in the fall, the shallower thermocline shoals the counter-current. The counter-current is also stronger on the western side of the channel throughout the year. Figure 2.9 also shows the strongest dynamical activity overall between the surface and 70m. Figure 2.10 shows the mean seasonal velocities for the upper 70m across the entire HIOG grid. The velocities are weakest in the winter and then grow through the summer before weakening again. The direction of flow shifts through the seasons as well. The flow, most likely driven by the HLCC, is

westward flowing through the region in the summer, but it weakens in the fall and winter so by spring, the flow is more north and eastward through the Ka'iwi Channel.

Instabilities are a cause of mixing and they are especially dramatic around the coast of Oah'u. Baroclinic instability is an important source of mixing found in rotating, well stratified fluids subject to a horizontal temperature gradient (Vallis 2006). The source of energy for this type of mixing is in the available potential energy of original, zonally symmetric flow (Gill, 1982). Quantifying these instabilities is particularly relevant as they can be an indicator of internal tides or eddies. Charney (1947) and Eady (1949) looked at baroclinic instability in meteorological applications, specifically with a focus on understanding mid-latitude cyclones. Lindzen and Farrell (1980) suggest this simple approximate for determining maximum growth rate of baroclinic instabilities:

$$\sigma = \frac{.31 f \left(\frac{dv}{dz} \right)}{N},$$

N represents buoyancy frequency, calculated as $N = \sqrt{\frac{g}{\rho} * \frac{d\rho}{dz}}$, where g is the gravitational constant, -9.8m/s^2 and ρ is potential density. f is the coriolis parameter calculated as $f = 2 \Omega \sin \theta$.

The growth rate of baroclinic instabilities was calculated using mean seasonal data at the surface layer (Figure 2.12) as well as the depth averaged upper 70 meters (Figure 2.13). Both are telling as the upper 70 meters captures the mixed layer instabilities and the surface layer captures any surface reflections of internal waves. The growth rate suggests bathymetry significantly influences mixing. However, Carter et al. (2008) found the steep bathymetry of Penguin Bank and the coast line of Oah'u were not major sites for internal wave generation. E-folding time is the amount of time it takes for energy to increase by a factor of e, essentially to double. For this region, the

e-folding time was found to be 1.65 days, which compares well with Barth (1994) for regions dominated by frontal instability and the theoretical has a lengthscale of 30km. Figures 2.12 and 2.13, showing the surface and upper 70m respectively, both show the strongest growth rates in the summer, which slowly dissipate through the fall and winter and are weakest in the spring. In the upper 70m mean data, the impact of Penguin Bank shallows is much more evident across the seasons. Both figures show higher instability off the south, south-east shore of Oah'u. The strong summer season in both figures suggests a built up rate of instability along the southern boundary of the model. This is more likely an effect of the boundary condition. Instabilities that build in the nested grid that are not captured by the parent grid will not pass through the boundaries.

One technique available to quantify sources of horizontal mixing is the Okubo-Weiss parameter, which is a relation between strain and vorticity. Strain is a measure of deformation, measured as: $S^2 = (\partial_x u_x - \partial_y u_y)^2 + (\partial_y u_x + \partial_x u_y)^2$ (Gill 1982). Vorticity is a measure of a body's rotation, determined by the curl of the velocity field, $\omega = \nabla \times v$. The Okubo-Weiss parameter is a relative comparison of the two properties defined as: $Q = S^2 - \omega^2$ (Okubo 1970, Weiss 1991). If Q is positive, the velocity field or water mass is dominated by strain and if it is negative, the field is dominated by vorticity.

For this study site, mean annual depth averaged data from the HIOG grid was used to investigate the role of strain and vorticity in the mixing. Strain dominates in shallower areas where deformation is more prevalent. Figure 2.14 reveals strain dominates the region primarily over Penguin Bank and in some of the shoreline waters of Oah'u. Generally strain is dominant along steep bathymetric contours. In all other areas, where bathymetry is not a dramatic feature, vorticity is dominant.

Vorticity is especially more dominant along headlands, as seen around the tip of Molokai, Penguin Bank and headlands along the Oah'u shore.

2.5.1 Ka'iwi Channel Transport and Current trends

Transport is a measure of water volume movement, through a planar section, measured in Sverdrups (Sv), $1\text{Sv} = 10^6\text{m}^3/\text{s}$. Transport was calculated across the Ka'iwi Channel using the same transect as the seasonal current profiles in Figure 2.15. The transport time series was detided using the seven major tidal constituents found near Hawai'i to determine the percent of variance explained by those constituents. The tidal ellipses (Figure. 2.8) in the channel show the currents flow almost exactly through the channel route and the tidal analysis supported that finding with the seven major constituents accounting for 84.89% of the variance through six years of data. The residual transport is shown in Figure 2.15. Grid markings show the annual breaks. This figure suggests there is some seasonal trends though they are not consistent every year. Most years the winter shows some negative transport indicating westward flow is dominant. The middle part of the year from late spring to early fall shows predominantly positive transport, indicating eastward flow.

2.5.2 OTEC site Analysis

An OTEC site is under consideration for a potential 100MW pilot plant located off the south coast of Oah'u, nearly directly south from Barber's point as seen in Figure 2.1. Ocean thermal energy conversion uses the Rankine cycle, a process which employs the temperature differences between cooler deep ocean water and warmer shallow water to drive a heat engine and extract kinetic energy via turbines. This energy drives generators and produces electricity. For the analysis of this site within the model, data was used from the grid location of the site plus fifteen cells in each direction, for a study area approximately 16.5 km^2 in size.

To analyze the background flows in this area, mean seasonal and annual data were analyzed. The OTEC site bathymetry is influenced primarily by Oah'u, as it is tapering to an abyssal plain away from the island. While still in relatively close proximity to the island, the site has a mean maximum depth of 1150m. The water column variability is stable over time as seen in Figure 2.16, a Hoffmueller plot of potential density. To determine the depth for the outflow, data from a plume model from the west coast of Oah'u, near Ko'olina was used (Rocheleau, personal con). Rocheleau's research suggested outflows be placed near 20K. Using mean data from the model, the depth of the 20K isotherm in the OTEC area is 140m, so the model outflow is placed there. Using the mean salinity of the outflow water from 755m cold water input, and the outflow temperature of 20K, the density of the water at the outflow was determined to be 1024kg/m^3 . The plume settled to the average depth of that density, 215m. The current structure at that depth, indicates the flow across the disposed water is westerly with some stronger currents reflecting around Penguin Bank as seen in Figure 2.17.

Figures:

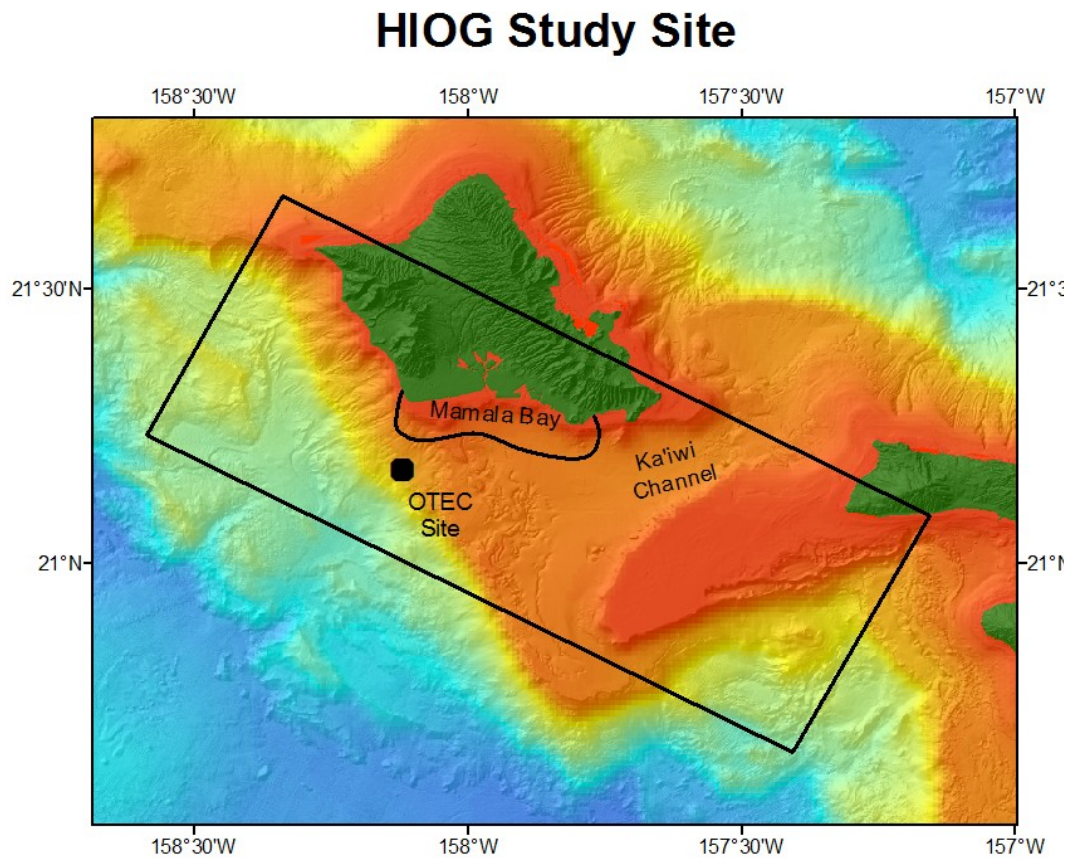


Figure 2.1. Bathymetry plot of Oah'u Regional Grid Study Site: Bathymetry plot of study site (boundaries are in black). Additional forecasts assessments were completed in Mamala Bay and at a potential pilot OTEC site

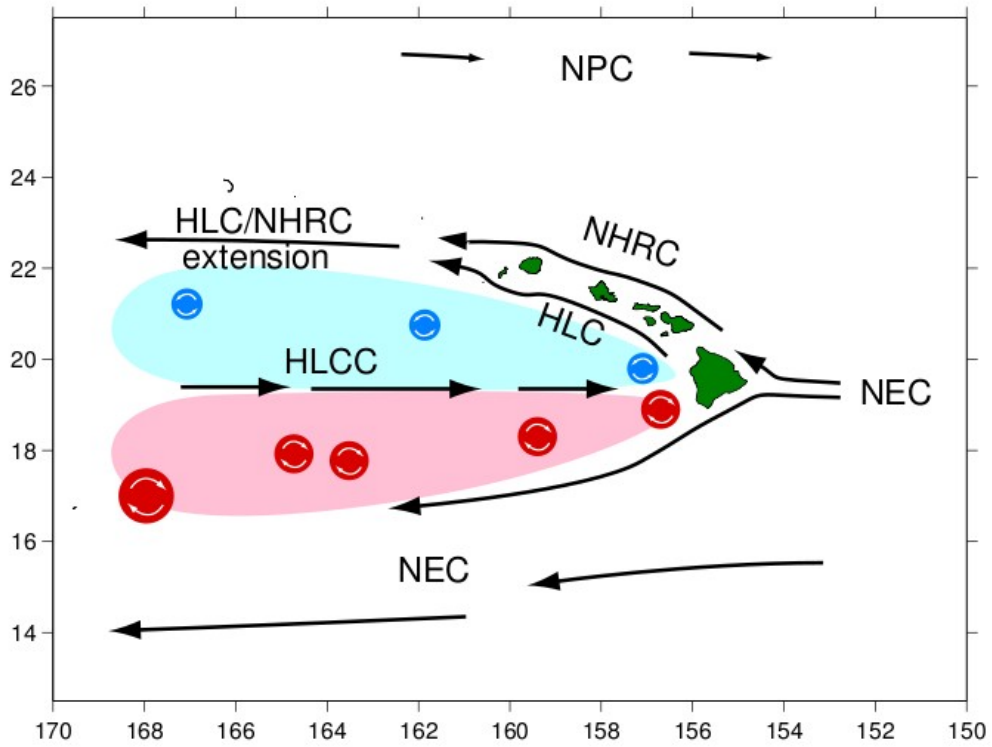


Figure 2.2. Canonical Circulation around the Hawaiian islands from Lumpkin (1998). Vectors indicate surface current direction. Magenta indicates area of anticyclones and blue indicates area of cyclones. See text for further description.

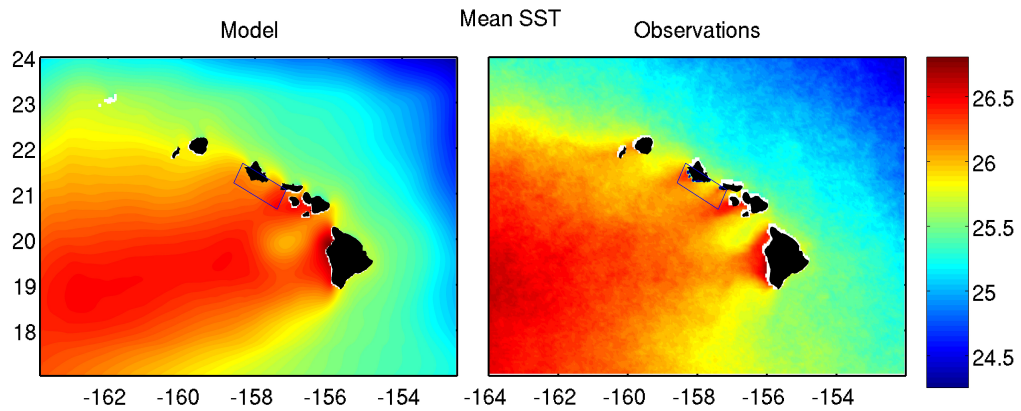


Figure 2.3: Mean annual temperature comparison between satellite SST data and ROMS SST data. The right plot shows the satellite observational data and the left plot shows ROMS temperatures. The large boundary displays data from the outer Hawaiian Islands grid. The blue boundary near Oah'u represents the boundary of the Oah'u regional grid and the data inside the box is from the Oah'u child grid. This is consistent with the larger grid. The temperature color bar is on the right in K.

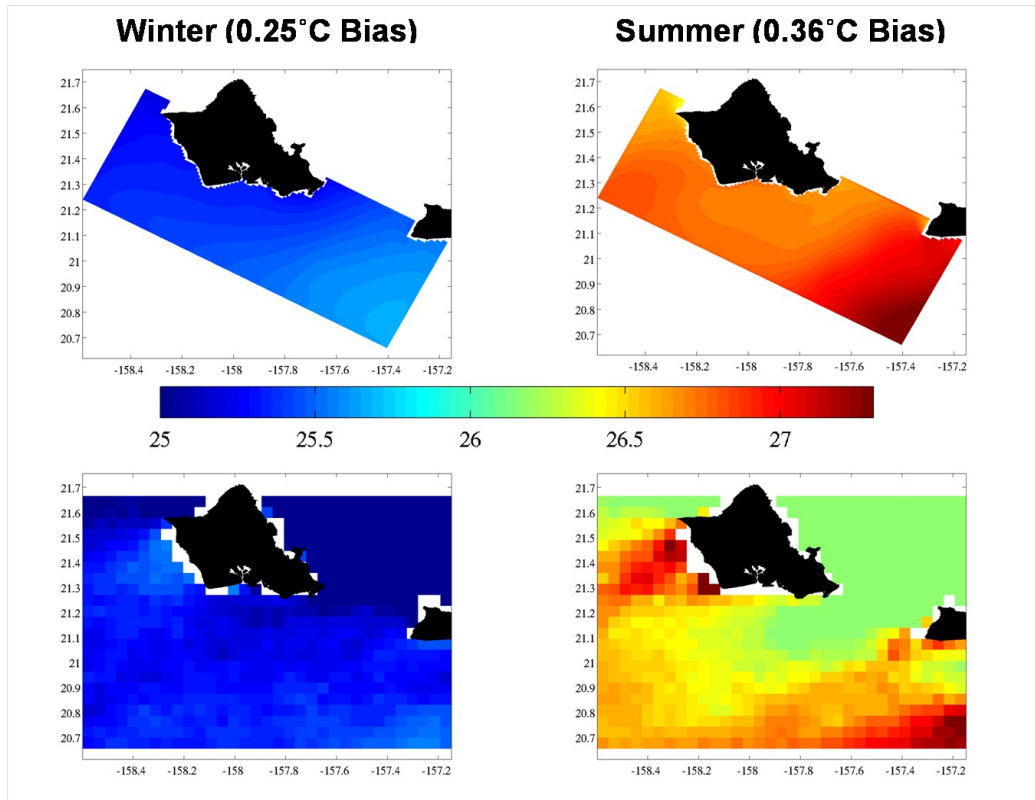


Figure 2.4: Mean winter and summer SST comparisons between the Oah'u regional grid and satellite data. The top two plots show model temperatures for winter (left) and summer (right). The bottom two plots show satellite temperatures for winter (left) and summer (right). Seasonal biases are shown in the seasonal label.

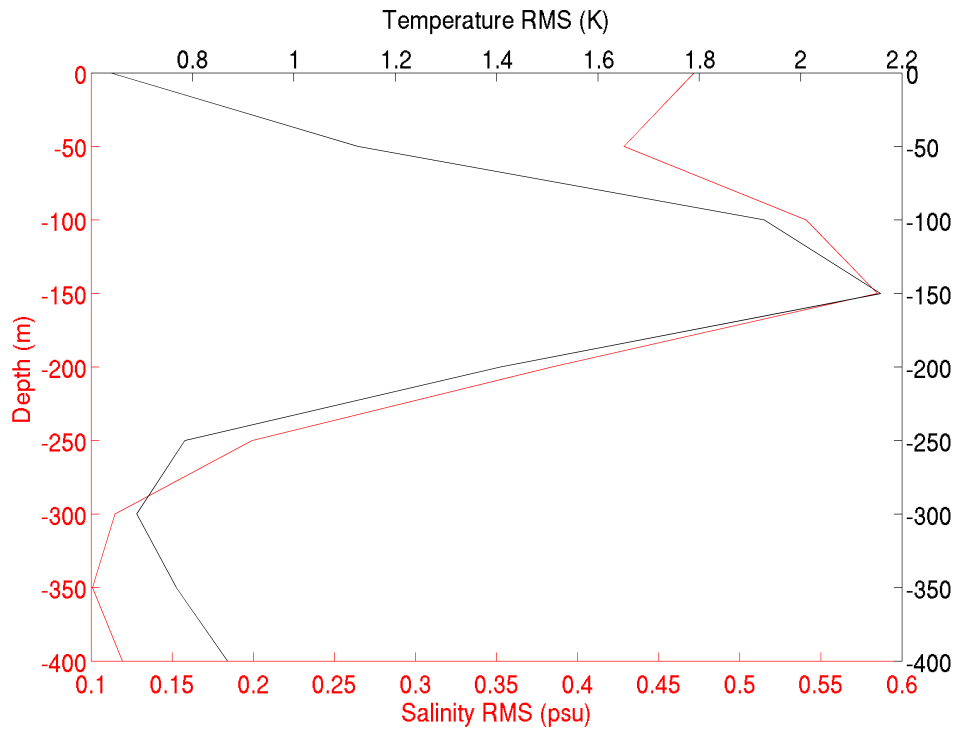


Figure 2.5: RMS of temperature and salinity between Seaglider observational data and ROMS data. Glider data is from deployment between April and August 2008 and ROMS data is compared from the same period. Data is binned by 25m depth intervals for RMS comparison.

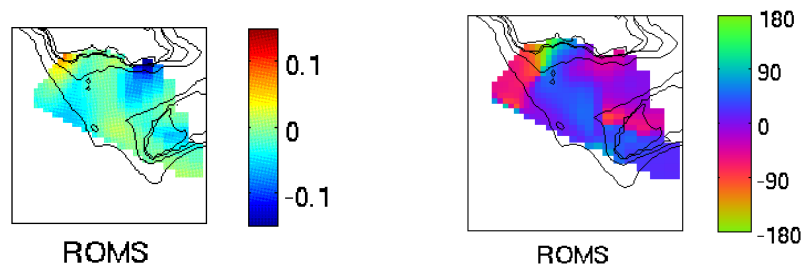


Figure 2.6: Differences between HF Radar and ROMS M_2 tidal amplitudes (left) and phases (right) of radial currents from Cass (2010).

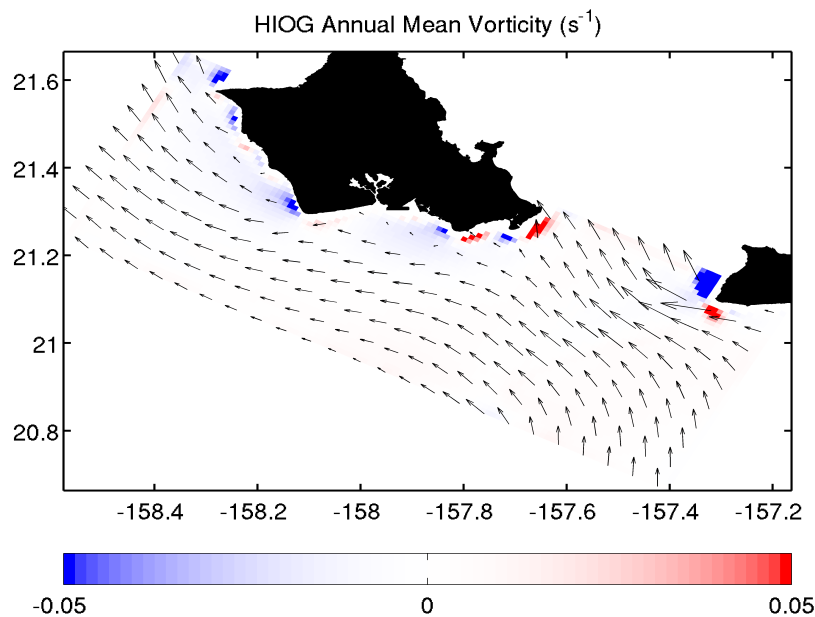
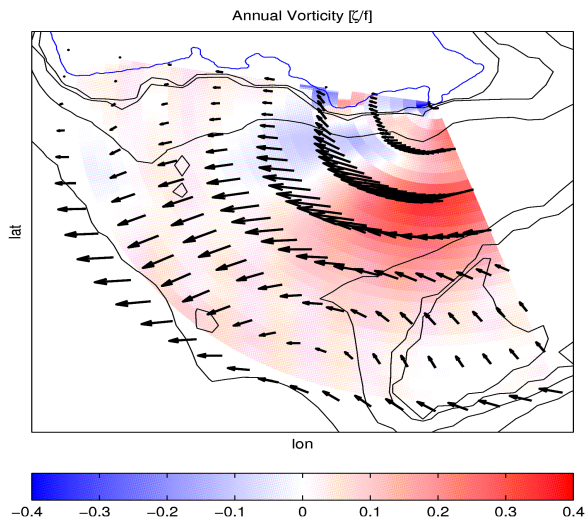


Figure 2.7: HF Vorticity Comparison between HF Radial data and ROMS velocities. Top plot is from Cass (2010) and represents annual vorticity magnitude with color bar and radial inferred velocity vectors overlaid. The bottom plot represents ROMS mean annual vorticity with velocity vectors overlaid. The velocity flow is consistent. Vorticity magnitude is smaller for ROMS but the trends are similar, with negative vorticities on the west side of the headlands and positive vorticities on the east side.

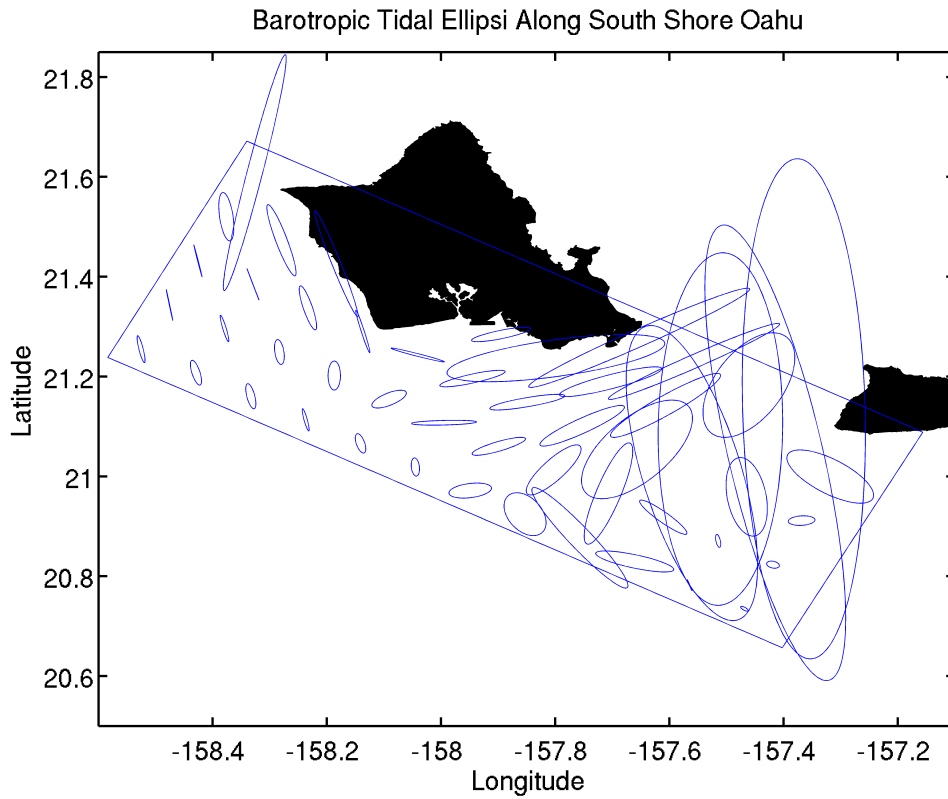


Figure 2.8: M_2 Barotropic Tidal Ellipses calculated using mean velocities from 2008. Tidal ellipses plotted every 10 grid cells. Ellipses generally oriented along shore and larger over shallow Penguin Bank east of Oah'u and over Kaena Ridge west of Oah'u. Ellipses also oriented nearly directly through the Ka'iwi Channel between Oah'u and Molokai.

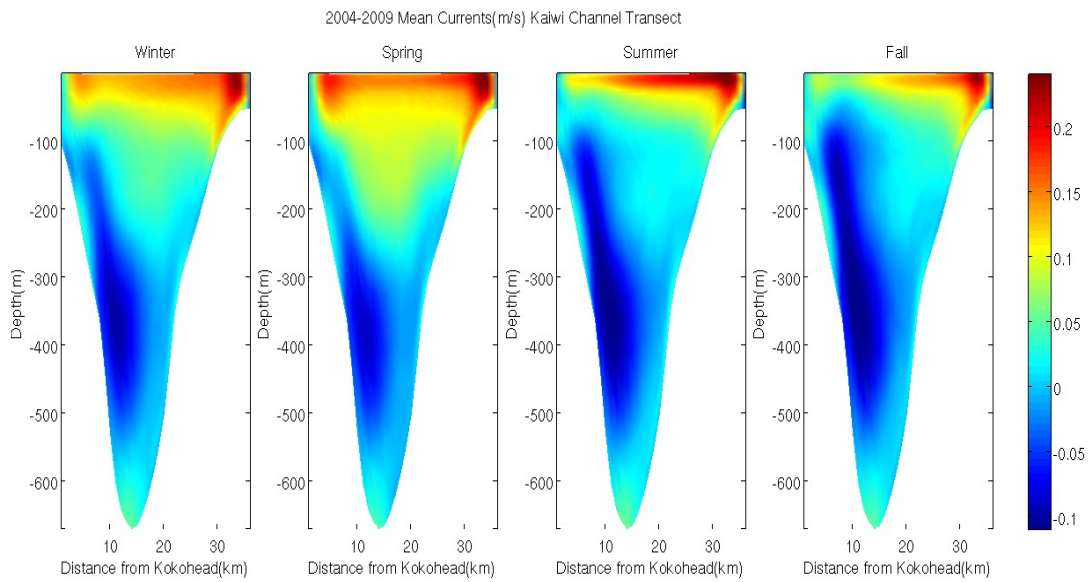


Figure 2.9: Ka'iwi Channel seasonal mean velocity transects. Transect runs from Kokohead (left) to Molokai (right). Colorbar indicates velocity magnitude with red indicating flow into the page (eastward) and blue indicating flow westward. Note dynamic layer in upper 70m, shift in velocity direction through depth seasonal magnitude change from summer to winter.

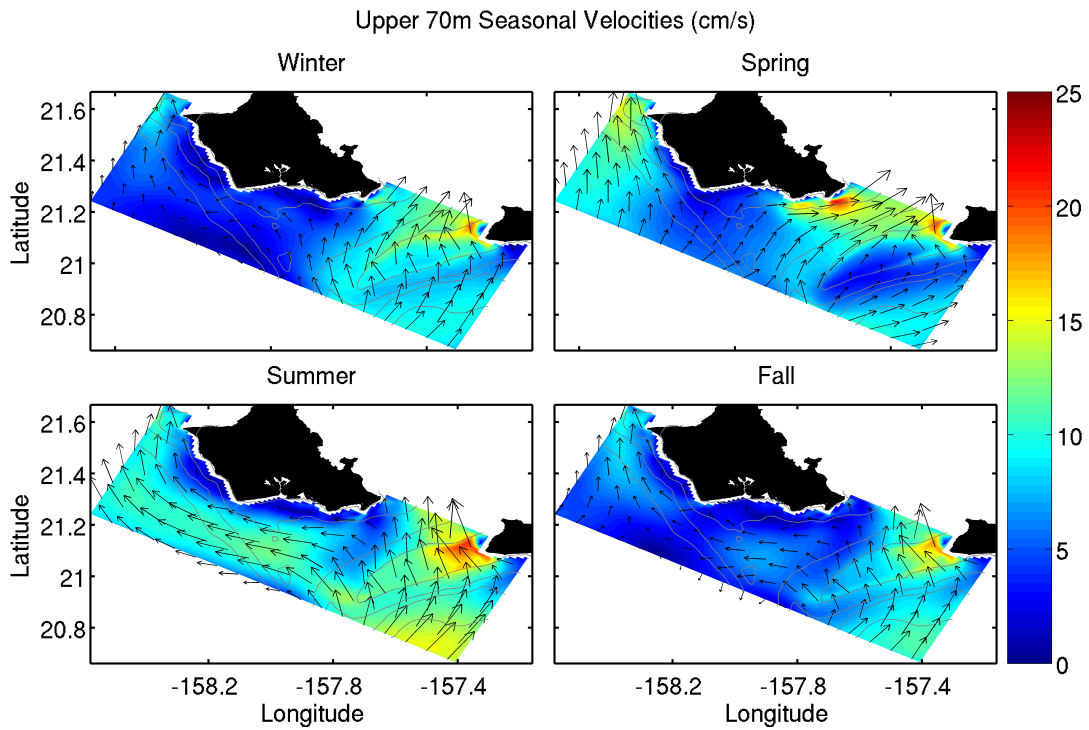


Figure 2.10: Mean seasonal velocity structure for upper 70m. Colorbar indicates magnitude and vectors indicate both direction and magnitude, with longer vectors indicating stronger magnitudes. Flow shifts from westward to eastward flow near the east coast of Oah'u between summer and winter though the impact seems to lag so it the greatest differences are seen between fall and spring.

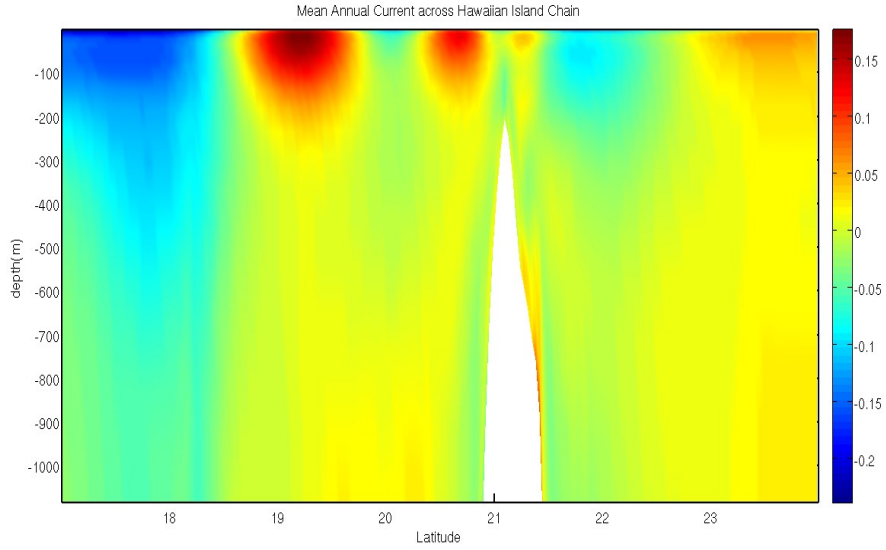


Figure 2.11: Outer island grid transect from south (left) to north (right) through the Kai'iwi Channel using Mean Annual velocities in the u-direction (east-west). Positive magnitude indicates flow from west to east and negative is from east to west. Blue and red flows show the canonical current patterns and the depth that they reach. From left to right, major flows NEC, HLCC, HLC, NHRC and the North Pacific Current can be seen, with the white space indicating the shallow depth of the Kai'iwi Channel.

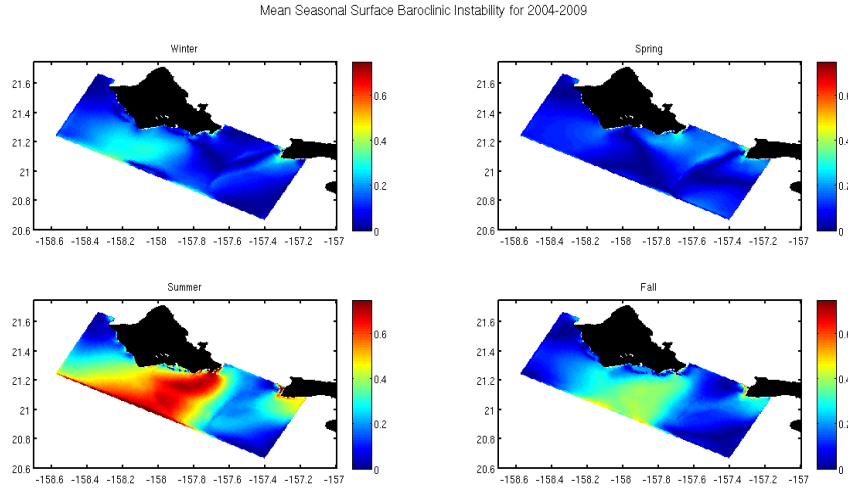


Figure 2.12: Mean Seasonal Surface growth rate of baroclinic instabilities. Calculated using the Eady index, it represents where the possibility for greatest conversion from potential to kinetic energy can be seen, with red indicating a high possibility.

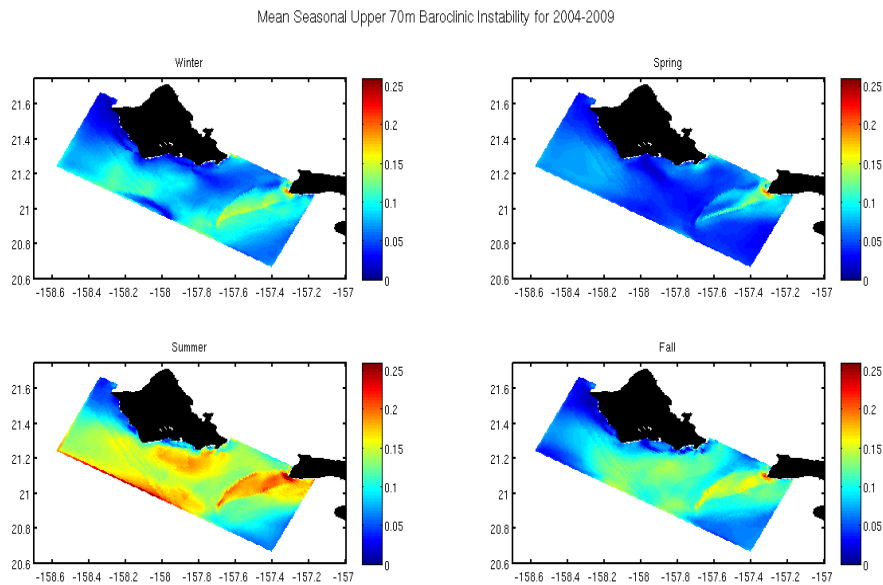


Figure 2.13: This shows the growth rate of instabilities for the upper 70m. This suggests more variability of instabilities across the region over each season, but a lower overall rate of instability relative to the surface.

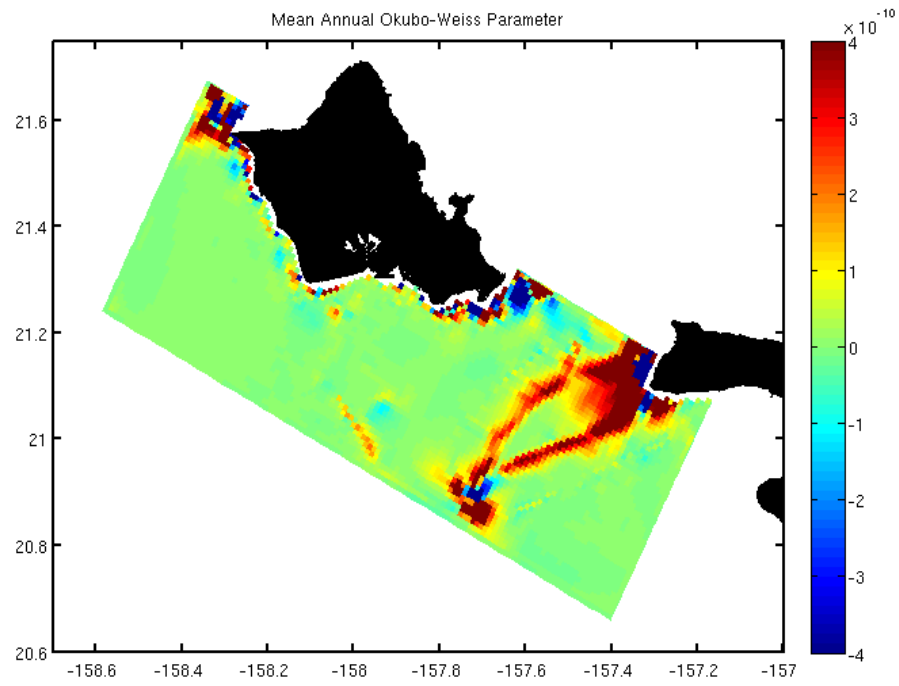


Figure 2.14: Okubo-Weiss represents the difference between vorticity and strain. Positive values indicate strain dominance and negative values indicate vorticity dominance.

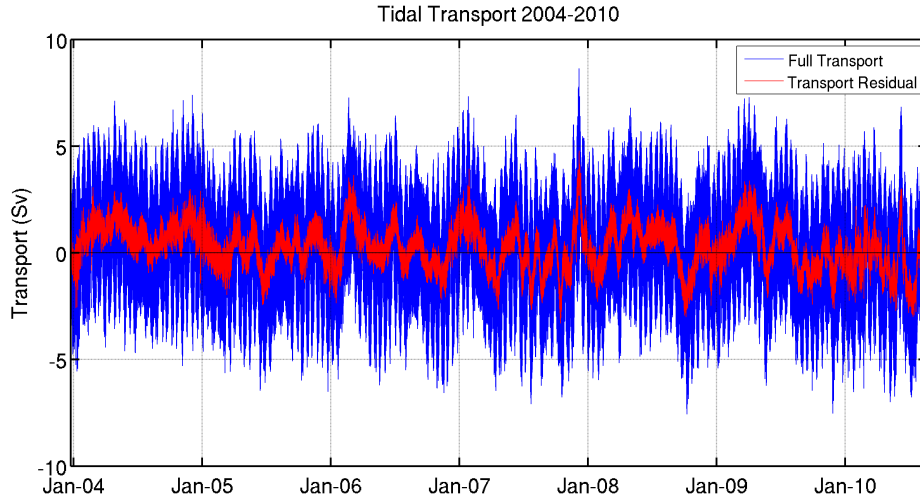


Figure 2.15: Tidal transport from 2004 – 2010. Blue indicates transport before major tidal constituents were removed and red indicates the residual transport after major constituents, M_2 , S_2 , K_1 , O_1 , K_2 , N_2 , and P_1 , were removed.

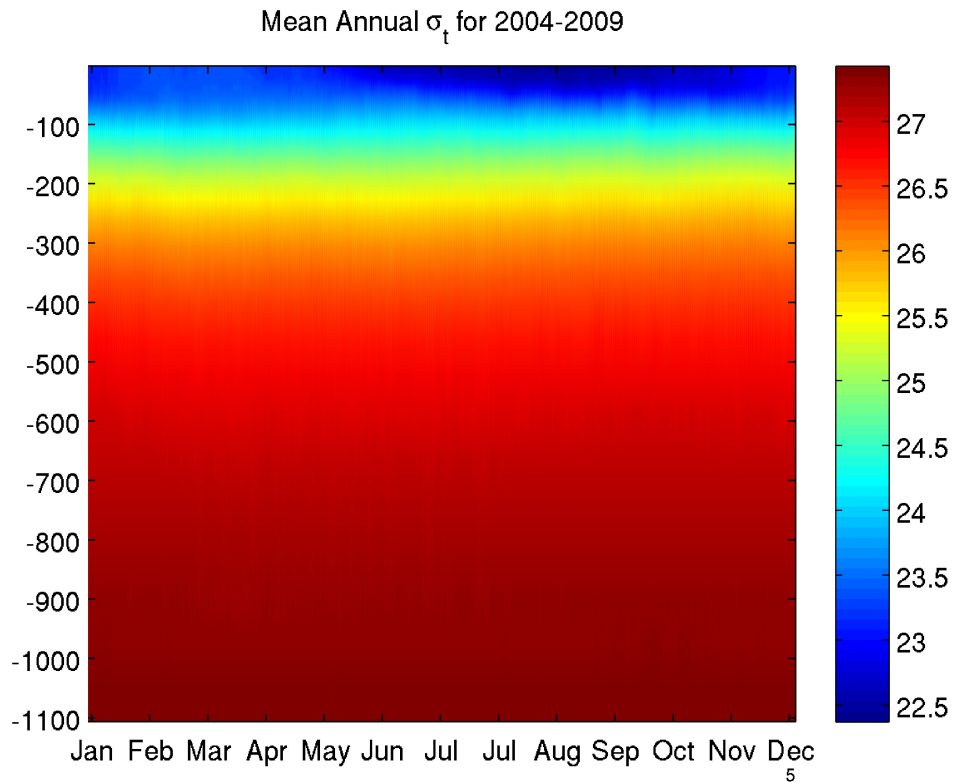


Figure 2.16: OTEC σ_t . Spatial mean of σ_t across OTEC region, through depth and throughout the year. Annual hoffmueller represents average from 6 years of data.

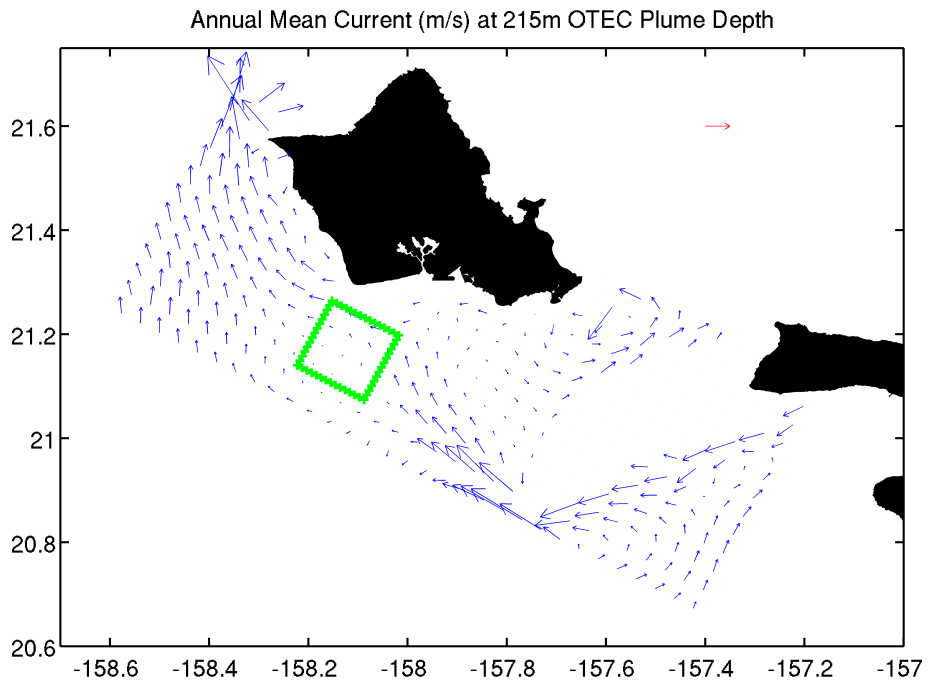


Figure 2.17: OTEC Annual Mean Currents(m/s) at Plume Depth with reference current vector in red of 5cm/s. OTEC region indicated in green.

Tables:

2.1. Honolulu Tide Gauge/ROMS Amplitude, Phase and RMSE:

HNL Tide Gauge Comparison			
	M2	S2	K1
Tide Gauge Amp (cm)	17.53	4.83	15.15
Model Amp (cm)	15.09	5.11	15.29
Tide Gauge Phase (deg)	60.69	58.98	227.66
Model Phase (deg)	67.07	62.30	233.97
RMSE (cm)	2.15	0.29	1.19

Table 2.1: Top three tidal constituent comparisons between tide gauge and modeled data. RMSE explained in section 2.4.1.

Chapter 3

Methods

The motivation for this study is to determine which observing systems have the greatest impact on the skill of the ROMS forecast around the south shore of Oah'u. For this study, an OSSE experiment with a twin approach is used in order to consider observing sensors not currently in the area, to produce a more thorough and robust assessment of observing systems.

3.1 Twin Experiment

Traditionally, model forecasts can only be evaluated by comparison to *in situ* sensors. This is limiting because the accuracy of the model can only be assessed where an *in situ* observation is available, and the impact of observations on dynamics across the whole grid can not be assessed as easily. For this work, we use a twin experiment to examine the role of the observing systems. With a twin experiment, a forward state estimation is created using the model with a designated set of forcing, boundary and initial conditions. A subsequent twin run is created maintaining all forcing from the truth with the exception of differing initial conditions. Both the forward and twin ocean states throughout time and space are known allowing full comparison to assess observing sensor impact on model forecast accuracy through space and time.

3.2 4DVAR

Data assimilation experiments are completed in this study using four dimensional variational data assimilation (4DVAR). Observations provide valuable sampling of the ocean but they are spatially and temporarily limited by the capabilities of the sensors. Models are valuable but without input from observations, they can only approximate ocean state. Data assimilation is the process of combining observations with a model to produce a better ocean circulation estimate than either would generate individually (Powell et al., 2008). The motivation of assimilation schemes is

to dynamically minimize the difference between model state and observations. A secondary motivation is to maintain consistency between dynamics and analysis, while still minimizing computational cost to make the assimilation as efficient as possible (Le Dimet and Talagrand 1986). It uses the full dynamics of the system to compute the sensitivities to observations, which are used to minimize the difference between the observations and the model. ROMS-IS4DVAR (Incremental Strong constraint 4DVAR) was developed based on the incremental techniques discussed in Courtier et al. (1994) and Weaver et al. (2003). Its predecessors, optimal interpolation(OI) and 3DVAR vary by assuming persistent dynamics. Specific details of the implementation of IS4DVAR in ROMS are found in Powell et al. (2008), but an overview is presented to aid in discussion of assimilation experiments.

We designate Ψ as the ocean state vector, containing model prognostic variables at all grid points as well as boundary conditions. ROMS uses seven standard prognostic variables, $(\zeta, u, v, \bar{u}, \bar{v}, T, S)$. ζ is the dynamic height (m), u and v are zonal and meridional velocities(m/s), \bar{u} and \bar{v} are barotropic velocities (m/s), T is potential temperature ($^{\circ}\text{C}$) and S is salinity (psu). The state evolution is accomplished by the integration of the nonlinear model:

$$\frac{\partial \Psi_{n+1}}{\partial t} = N(\Psi_n) + f_n,$$

where Ψ_n is a time-dependent state and f_n is the nonlinear forcing term. It is assumed that the NLM replicates the ocean state well enough that only small linear increments, $\delta\Psi$, to the state are required to deviate from the non-linear trajectory to a new trajectory that is closer to the observations (Powell et al. 2008). The incremental trajectory is determined from the integration of the tangent linear ROMS (TLM) equation (Lacarra and Talagrand 1988, Moore et al. 2004). The initial conditions, atmospheric forcing and boundary conditions are all part of the control vector and are dynamically adjusted. The adjoint ROMS (ADM) component is used with the TLM to analyze model sensitivity. It provides the sensitivity of the system to variations in

the model state vector (Moore et al. 2004). For an incremental approach, a quadratic cost function is used to minimize perturbations to circulation.

$$J_0 = \frac{1}{2} \sum_{i=0}^{N_{obs}} \left(H'_i \delta\psi(t_i) - d_i \right)^T O^{-1} \left(H'_i \delta\psi(t_i) - d_i \right),$$

$$J_b = \frac{1}{2} \delta\psi(0)^T B^{-1} \delta\psi(0),$$

$$J = J_o + J_b,$$

J_0 is the observation cost function where \mathbf{O} represents the observation representative error covariance and d_i represents the innovation vector, or the difference between the measurement vector and the modeled measurement vector. Since the observations, by definition can not sample enough to fully constrain the model, J_b provides the additional background constraint to limit the size of the increments and \mathbf{B} is the background error covariance. Together, they represent the total cost function. One of the benefits of the TLM and ADM today is that the multiprocessor computers allow for much greater computational complexity (Moore, 2004). Ocean systems are still such a large dimension problem the solution to minimize J cannot be computed directly, rather, it must be approximated via conjugate gradient procedure. In the inner loops the TLM propagates the increments forward in time to evaluate J_0 (Broquet, et al. 2009). The outer loops are only used to ensure non-linear effects that occur during assimilation are incorporated into the NLM trajectory (Powell et al. 2008). For this experiment, we use 4DVAR adjusting the initial conditions as well as the boundary conditions and atmospheric forcing in time over the window. Because of the complexity of this region and the strength that these forcings have on our HIOG region, this serves as an ideal testbed for examining how well predictions can be performed in the realm of dominant external forcing.

3.3 Observing System Simulation Experiments (OSSE)

Observing system simulation experiments are used to assess the impact of hypothetical data on a forecast system. They are conducted by selectively removing observing systems from a model simulation run to analyze the impact of their absence on the model forecast. If the impact from a sensor is negligible, that sensor may not provide useful information to the model's forecast. However, if the absence degrades the forecast significantly, it can be concluded that the sensor is valuable for that forecast.

Bouttier and Kelly (2001) conducted OSEs in the European Centre for Medium-Range weather forecasts (ECMWF) 4DVAR system. Uden et al. (1997) conducted OSEs with 3DVAR. Both studies found some observations to be valuable in certain areas and not in others. Additionally, Bouttier and Kelly had areas which were so data rich, that they were not able to extract all of the observation information for inclusion in the data assimilation.

3.4 Experiment Setup

For this study, HIIG is used in tandem with its nested child grid, HIOG to conduct the OSSE. The forward run of the twin experiment is from the period January 1 to June 30, 2009 taken from the model run evaluated in section 2.5. The twin was created by integrating the same period but started from climatology. This created two similar but distinct circulations for the twin experiment.

Allowed to run infinitely, the twin forced by the same atmosphere and boundary conditions of the twin state estimate, will eventually return to the forward state, making it impossible to analyze the impact of the observations. An RMS between the twin state and forward model for HIIG reveals that for the experiment length of six months, the twin does not converge to the forward. In HIOG however, the twin can converge in less than fifteen days, so it is necessary to use the twin HIIG model to ensure boundary conditions provide a different solution from the forward. The result

is that in the twin OSSE performed in HIOG, even when all the observations are assimilated, the twin will never reach the twin state estimate, because it has different boundary forcing. This is similar to operational systems where global models provide only larger-scale estimates of the flow. Therefore in the analyses, each OSSE case is compared against the full observation case.

3.5 Synthetic Observations

To generate synthetic observations, the twin state estimation is sampled in the same manner each observing system would sample the ocean. The sampling method used to best replicate each observing system is discussed below. All of the sensors provide unique information for the model. Figure 3.1 displays all of the sensors' coverages, except SST, which covers the entire surface. The OSSE will examine how these sensors provide benefit to the model forecast.

For HIOG, each Jason satellite passes through the grid once during a full 10-day orbital cycle. The synthetic sensors were designed to mimic the Jason parameters, so they sample the ocean grid at the same temporal resolution and pass across the grid in the same place as the real Jason satellites do.

Synthetic SST satellites were designed to sample the entire HIOG grid twice per day. While in the real ocean this time varies slightly each day, for uniformity, 0000 and 1200 GMT (1000 and 2200HST) were used for the synthetic satellite sampling times. It would ordinarily take a couple of seconds to make the entire pass through this grid, but for this experiment, it was assumed that the entire grid was sampled simultaneously as this is less than the time-step of the model.

Synthetic HF transmit and receive stations were placed at Kokohead, Barbers Point and Kaka'ako Park. The ranges and bearings of coverage for Kokohead and Kaka'ako

were determined from data from the stations in operation at those locations. Barbers Point was in the installation phase during these experiments, so expected coverages were used based on theoretical experiments by Dr. Pierre Flament. Barbers Point will have taller antennas, which allow greater coverage, than either of the other two. It is not normal to Kokohead, but the Kaka'ako site allows resolution of the radial vectors to infer surface currents. Though they can be set up to sample as frequently as desired, a 15min sampling interval was chosen for the synthetic observations. To minimize noise from the 15min samples, 3 hour mean radial signal data from the 15min samples were assimilated.

A synthetic glider was set up to run continuously between Kokohead and Penguin Bank. Designed to sawtooth and follow the same route a regular glider would, it went back and forth between $21.25^{\circ}\text{N}/-157.7^{\circ}\text{W}$ and $21.15^{\circ}\text{N}/-157.51^{\circ}\text{W}$ throughout the six month OSSE period. It was set up to sample every 5 min although a glider could sample more frequently if desired.

Lastly, a synthetic mooring was placed at approximately the deepest center of the Ka'iwi Channel at $21.21\text{N}/-157.56\text{W}$ to provide constraint near the model's open boundary. Temperature and salinity sensors were placed every 10m between 30 and 180m and a current profiling sensor was placed every 20m between 20 and 500m. The mooring sampled the model hourly.

To make them as realistic as possible, an error is applied to each observation. The errors of representativeness applied are more a measure of mean variance and not representative of actual observing system errors. They are selected to be as realistic as possible such that they represent the error the model has in representing that observation. The perturbation is applied using a two step process. Errors representative of the sensor errors, listed in Table 3.1, are multiplied as a function, to

apply a random error to the observations. Secondly, a certain percent (also found in Table 3.1) of each type of observation is dropped to represent realistic data loss. These newly perturbed observations are then established as permanent twin state observation values for every OSSE.

To understand how much each observing system is actually measuring of the ocean, an analysis of coverage is shown in Table 3.2. Even with fully synthetic observations, only 1% of the ocean state over four days is observed on average. The breakdown shows how much each individual observing type contributed to the total amount of coverage. This demonstrates that even in a twin experiment, when one is able to have a somewhat higher than likely quantity of observations available, still only a small percent of the ocean is being sampled.

3.6 OSSE Test Cases

The baseline that all OSSE cases are compared against assimilates all available synthetic observations into the twin. Subsequent runs are completed with the following observing systems withheld; all satellites, all HF Radars, mooring, and glider. Since ocean activity can be swept away in less than fifteen days in HIOG, forecasts are designated to be only four days. As each OSSE run is completed, forecasts were made for the subsequent four days throughout the six month run resulting in a total of 41 forecast cycles.

Forecasts created during the assimilation of each test case are compared to the full assimilation to assess sensor impacts. As with other OSSEs, it is assumed assimilating all of the observations produces the best forecast and the most accurate state of the ocean for assessment. After all runs were completed, we analyzed Mamala Bay, the OTEC site and the entire modeled grid to investigate the impacts of the sensors on forecasts of each area. As previously shown, the surface layer extends

to 70m so for Mamala Bay we examine the upper 70m layer and the 70-150m layer. The OTEC site was assessed at the plume depth of 215m. The upper 70m dynamic layer of the entire HIOG grid was also assessed to see how the observations affected the model beyond the temporal and spatial coverage of the sensors.

Data were analyzed both temporally and spatially. For the temporal analysis, the first two cycles of forecast data were dropped to ensure no residual effects from the run initialization. Forty-one, four day cycles were included in each assessment. Both correlation and RMS statistical analyses were used. Each technique helps elucidate potential causes for variation in the OSSEs. For each statistical assessment, median values, from the 41 cycles, for each time step through the 4 day forecast cycle were extracted to discern trends through the forecast period. Included with the results of each OSSE case is the 'background', which represents the twin model run with no data assimilation. Throughout most of these analyses the background has the greatest deviance from the truth, and is presented to show the improvement observing systems offer.

In addition to spatially averaged temporal analyses, temporally averaged spatial RMS and correlation analyses are used to evaluate where observing systems impacted the forecast. The spatial analyses are presented to identify where the model is improved by each observing sensor and to help illustrate why that might be the case. Spatial figures are presented as impact figures. For depth layers, the values are depth averaged for each point in space first. Next the RMS or correlation is calculated for each grid point, through the full timeseries, between each OSSE forecast run and the full state estimation run, in which all observations are included. Impact is then calculated by removing the RMS of the all observations case from each of the cases in which an observation was withheld. The remaining signal represents the impact of each observation on the model forecasts from the 6 month run. Spatial RMS and

correlation plots reveal where the greatest area of impact is. In the case of correlation, the withholding cases are removed from the all observation case, such that a positive impact value indicates the observation type is improving the forecast in either the RMS or correlation.

To further study the influences of sensors on internal wave activity and mixing in the model, baroclinic instability and the vorticity-strain parameter were used. Both were calculated in the same manner as section 2.5. The impact was calculated in the same manner as the RMS and correlation impact parameters were.

Figures:

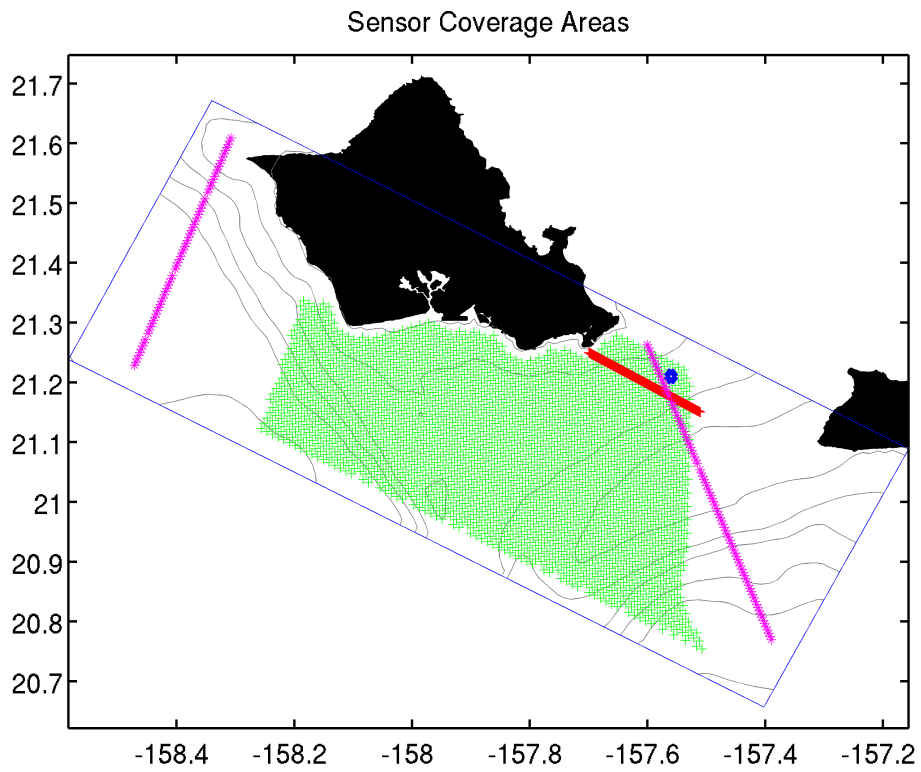


Figure 3.1: Coverage area of synthetic observing systems used for OSSEs. Purple lines represent synthetic SSH satellites; Green area represents synthetic HF Radar coverage; Red line represents synthetic glider route; Blue circle marks synthetic mooring location.

Tables:

Table 3.1

Sensor	Type	Error	% Randomly Dropped Values
HF Radar	Radial	0.0081	25
Glider	Temperature	0.0900	5
	Salinity	0.0016	5
SSH	Zeta	0.0006	5
SST	Temperature	0.0100	35
Mooring	Temperature	0.0900	5
	Salinity	0.0016	5
	U	0.0081	5
	V	0.0081	5

Table 3.1: This table shows how the synthetic observations were developed. The error was applied to all synthetic observations after they were sampled. Then, a percent of the observation values is dropped at random to represent the error we think model has in representing the observation. It is determined from mean variance more than actual observation errors.

Table 3.2

Observing System Sampling Coverage	
Average % Sampled	~1%
Of that ~1%, observing system breakdown was:	
HF Radar	%79.7
Satellites	%14.2
Mooring	%4.7
Glider	%1.4

Table 3.2: Table shows how much of the model is sampled during every four day cycle and of that Average % Sampled, how much is sampled by each observing system.

Chapter 4

Results / Discussion

To conduct the OSSE, four test cases were created by withholding HF radar, satellites, glider and mooring data for comparison against the case in which all data were used. The forecasts from each case are compared in the HIOG, Mamala Bay and the pilot OTEC site regions, with both temporal and spatial analyses, to assess impacts of withholding observing systems on each ocean forecast. Primary properties of interest are upper 70m temperature, upper 70m velocity and density (OTEC site only). These were chosen as representative metrics because they are indicative of the ocean state for each region.

RMS is used as an indicator of the forecast error. For the following results we identify each of the cases by the name of the observing system that was withheld. We present the difference in RMS between the full case (where all the observing systems are used) and the given case, as a measure of the observational impact. If the RMS is low for a given run, that implies that when that sensor was withheld it did not significantly affect the forecast and does not have a large influence. However, if the RMS is much higher when an observation is removed, that sensor is providing valuable information for the forecast of the property under consideration in the model.

We also use correlation as a metric of forecasting skill. Again, we difference the full case with the given case to determine the impact on correlation. A correlation near 1.0 is an indicator of high correlation. If, when an observation is removed, correlation does not appreciably change, it does not have a large influence on the forecast. However, if the correlation impact is high, that observing sensor had a more significant influence on the forecast. A negative correlation means the observing system made the forecast worse.

4.1 Full Model for HIOG

We begin our analysis by comparing forecasts of the entire model grid. We expect to identify which sensors have the strongest influence on the forecasts across the region and where in the region their influence is strongest.

4.1.1 Upper 70m Layer

The mean RMS and correlation for the time series represents the temporally averaged value between the state estimation, when all observations were used, and each forecast case. In Figure 4.1, the highest RMS and lowest correlation are observed when satellites are withheld. For the forecast case when all observations were included, the RMS was 0.20K. When satellites were removed the RMS doubled to 0.40K suggesting that the observation has an important constraint on the temperature. When HF radar was withheld, the RMS is 0.33K, which while not as high as satellites, is still significant. When the glider and mooring were withheld, independently, they each had an RMS of 0.31K, which while lower than the HF radar, is still significant. In the background case, when no observations were assimilated, the RMS is highest at 0.53K. The mean correlation when all observations were included was 0.95, which like RMS, was the best case scenario. The mean correlations when observations were removed were fairly similar to one another. When HF radar, the glider or the mooring were removed, the correlation dropped to 0.93, but withholding satellites lowered the correlation to 0.92. When no observations were included, the correlation of the background was 0.59. Satellites, most likely SST, have the greatest impact, 0.20K, on the temperature forecast in the upper 70m. HF Radar has a smaller impact of 0.13K, while the glider and mooring have impacts of .11K. Most importantly, all the observations improved the forecast by at least 55%.

Spatial impact plots were generated by comparing a daily timeseries through the experiment period at each point in the grid as explained in section 3.6. Spatial RMS impact of temperature (see Figure 4.2,) reveals satellites have the highest impact as great as .25K on the western side of the grid. HF radar shows positive impact in and around its immediate coverage area, including the coastal Mamala Bay area. The glider and mooring have localized positive impact in the area that they are sampling. They also show some negative impacts near the southern boundary of the grid and for the mooring on the south side of Makapu'u. This suggests that in these areas the observing system is actually negatively influencing the forecast. While the satellites do not have as strong an impact on the temperature forecast correlation (Figure 4.3), they still has the highest impact of the observation types. HF radar, glider and mooring correlations are also proportionally smaller than their RMS plots with higher impacts in the same areas. This suggests that the temperature background is well correlated and therefore withholding observations did not have as large an impact on correlation as it did on RMS.

Temporal velocity forecast cycle RMS and correlation results (Figure 4.4) reveal withholding of HF radar has the greatest impact on reducing the forecast error and improving the correlation. The mean RMS for the time series for the all observations case is 0.13m/s. When the glider or mooring were removed, the RMS was raised to 0.136m/s. When the satellites were removed the RMS was slightly higher at 0.144m/s, but the highest RMS, when the HF radar was removed, was 0.15m/s. For the background , the RMS was 0.24m/s. The mean correlation for the all observations case is 0.89. When the glider is removed, the correlation is 0.869. When the mooring is removed, the correlation is only slightly lower, 0.866. When satellites are withheld, the correlation drops to 0.856 and when HF radar is removed, it drops to 0.84 . The background correlation is 0.59. These cases converge by the end of the forecast cycle. The convergence will occur over time as the strength of

impact of each observation type will wane. While the removal of any observation still degrades the forecast, as seen in both the RMS and correlation, the amount of amount of influence converges by the end of the forecast cycle.

Spatially, the velocity RMS, Figure 4.5, shows the HF radar has impacts near 0.08-0.10m/s with a peak at the tip of Makapu'u near 0.13m/s on the upper 70m velocity forecast predominantly in the area that it samples. Satellites, while having a much lower overall impact than HF radar, still show impacts as high as 0.13m/s as seen with HF radar. However, these higher impacts are seen only over the Kaena Ridge on the western edge of the grid and at the southern tip of Molokai. This is likely related to the extremely dynamic activity taking place at both of these spots. The areas have steep bathymetry and higher vorticity near the headlands, making it difficult to both model and forecast. Consequently, the removal of even one of the observations has an impact on the forecast. The spatial correlation, Figure 4.6, shows HF radar impacts as high as 30. It is clear that each of the observations positively impact the model. All of the observations show a similar positive impact at the northwest corner of the grid over Kaena Ridge and at the southern tip of Molokai similar to the spatial RMS.

4.1.2 Spectral analysis

A spectral analysis of velocities was used to investigate how the sensors impact the model's resolution of tidal signals and energy density, and allow investigation into potential influences of baroclinic waves in the absence of constraint from the sensors. We analyzed the spectrum of time series of the u and v velocity components from the surface and the upper 70m of data. For the surface case, each spatial point was analyzed through the time series. Then the results were spatially averaged. For the second case, the data was depth averaged at each point first and then it followed the same process as the surface analysis.

Spectral analysis was done on the surface data and the depth averaged upper 70m. The mean upper 70m data showed almost exactly the same distribution of energy through frequency space as the surface layer data, but with lower overall energy magnitude. The surface spectral analysis, shown in Figure 4.7 reveals some variations when sensors are withheld, but the highest impact occurs when HF Radar was withheld. This case revealed higher energy near the subinertial frequency, which at this latitude (21°N) is approximately 33 hours. With the absence of constraint on the surface velocity field, the energy is able to move to the subinertial band, predominantly baroclinic currents, due to density changes.

4.1.3 Impact on Growth Rate of Baroclinic Instabilities

We investigated the observing system impact on the growth rate of baroclinic instabilities in the upper 70m layer. Growth rates (see Figure 4.8) were compared using the state estimation data for each case rather than the forecast data. The forecast is not as revealing as the state estimate when considering the growth rate because it is more representative when assessed over a longer period of time. HF Radar has the strongest impact on the growth rate. The impact is greatest over Penguin Bank and through the Ka'iwi Channel. The satellites showed a slightly negative impact on the growth rate in the same areas that HF Radar showed a positive impact. The satellites may have a negative influence if they are over constraining surface temperature leading to a homogeneity that is not actually there. The glider and mooring both show primarily positive but nearly negligible impacts on the growth rate of instability.

4.1.4 Strain-Vorticity Parameter

Okubo – Weiss parameter was calculated using barotropic velocities from the state estimation. This parameter, like the growth rate of instabilities, is better evaluated using the state estimate, rather than forecast data. Impact Figure 4.9 shows HF radar

positively impacts the capture of the strain influence on the northern side and southern tip of Penguin Bank. The satellites have a slightly elevated impact near the southern tip of Penguin Bank as well. All of the cases show similar impact on the parameter near the southern boundary of the grid west of Penguin Bank. This implies this is a model boundary influence rather than a sensor impact. Beyond the boundary, the mooring and glider have almost no impact on the capture of strain and vorticity using the Okubo-Weiss parameter.

4.2 Mamala Bay

4.2.1 Upper 70m

Temporal temperature RMS and correlation plots, Figure 4.10, in the upper layer of Mamala Bay show withholding satellites produces the highest RMS but withholding HF Radar produces the lowest correlation. The mean RMS for the time series for the all observations case is 0.29K. When the glider is withheld, the RMS is 0.303K, Withholding the mooring resulted in an RMS of 0.31K. When the HF radar is removed the RMS is slightly higher at 0.331K, but the highest RMS, when the satellites are removed, is 0.418K. For the background, the RMS is 0.476K. The mean correlation for the all observations case is 0.929. When the glider is removed, the correlation is 0.917. When the mooring is withheld, the correlation is only slightly lower, 0.913. When satellites are withheld, the correlation drops to 0.905 and when HF radar is removed, it drops to 0.902. The background correlation is 0.49. These results suggests that over time, the satellites improve the forecast of the model's spatially averaged magnitude of temperature, better than the radar. However, the radar improves the forecast of the model's spatial variability of temperature better than satellites. In these temporal figures, impact was not used, so these represent RMS and correlation directly.

The spatial RMS impact, Figure 4.11, shows satellites have a much greater impact than the other sensors across the entire Bay area, but HF radar is still significant, especially close to shore. The glider and mooring have nearly negligible impact in the upper 70m of Mamala Bay.

Temporal velocity RMS and correlation plots, Figure 4.12, shows the RMS and correlations both converge, but prior to that convergence, withholding HF radar has the greatest impact on RMS and correlation. The mean RMS for the time series for the all observations case is 0.132m/s. When the glider is withheld, the RMS is 0.140m/s, Withholding the mooring results in an RMS of 0.1439. When the satellites are removed the RMS is slightly higher at 0.147 but the highest RMS, when the HF radar is removed, is 0.153m/s,. For the background, the RMS is 0.174m/s. The mean correlation for the all observations case is 0.770. When the glider is removed, the correlation is 0.738. When the mooring is withheld, the correlation is only slightly lower, 0.725. When satellites are withheld, the correlation drops to 0.709 and when HF radar is removed, it drops to 0.679 . The background correlation is 0.49. Spatial RMS of velocity in Mamala Bay, Figure 4.13, shows HF radar has a positive impact, while satellites have only a small impact and the glider and mooring have no significant impact in the surface velocities in Mamala Bay.

4.2.2 70-150m

Temperature in the deeper layer of Mamala Bay (70-150m) showed more similar influences from each observing sensor (Figure 4.14) than the overall grid results. The mean temporal RMS values for temperature for all observations is 0.55K. At this depth, all of the observations have a similar impact on the forecast, but the highest RMS occurs when the mooring is withheld, at 0.64K. Next, withholding the HF radar produces an RMS of 0.63K. When the satellites are withheld, the RMS is 0.62K, and withholding the glider, the RMS is 0.60K. The background RMS is 0.78K. The mean correlations for each case are also very similar. With the all observations case,

the correlation is 0.96. When the glider is withheld, correlation is 0.951, and with the removal of satellites, 0.948. Withholding the mooring produces 0.947 correlation and withholding the HF radar, it drops to 0.94. The background correlation is 0.927. The RMS reveals that while the observations start off at varying magnitudes, they converge after 48 hours, due to the previously discussed waning impact of the observing systems over the period of the forecast cycle. Both the RMS and correlation are similar for each sensor. This similarity comes partly because it is a smaller area that is being sampled, but additionally, unlike the surface layer where satellites and HF radar dominate the forecasts, the sensors each play an important role constraining the model at this depth. Satellites and HF radar constrain the surface well, but this suggests some influence at depth. Both the mooring and glider sample in the water column and have a much higher likelihood of constraining the model at depth.

Figure 4.15 shows the spatial RMS of the Mamala Bay temperature. The HF radar has the strongest influence in the area, but all four sensors show some positive impact. The glider has the least influence, followed by the satellites. The mooring and HF radar show up to .15K and 0.4K impact respectively. The higher RMS impact is seen near the coastline for both sensors. The in situ mooring is able to constrain the model in a variable tidal, dynamic depth range. The glider samples the tides in time and space and tends to broaden the tidal spectrum, making it difficult to assimilate. Figure 2.6 previously showed the glider to have the highest RMS at 150m.

Temporal velocity forecast cycle RMS and correlation results for Mamala Bay, 70-150m (Figure 4.16) reveal withholding of HF radar raises the RMS and reduces the correlation more than any other. The mean RMS for the time series for the all observations case is 0.10m/s. When the glider is withheld, the RMS is 0.112m/s.

Withholding either the satellites or mooring results in an RMS of 0.114m/s, but withholding the HF radar is higher at 0.12m/s, The background RMS is 0.144m/s. The mean correlation for all observations is 0.82. When the glider is withheld, correlation drops to 0.78. Withholding the mooring, it lowers further to 0.771 and without the satellites, it is 0.768. It drops the most when HF radar is withheld and the correlation is 0.73. The background circulation is 0.49. These forecast cases also converge by approximately 72hrs.

The spatial velocity RMS for Mamala Bay, 70-150m, Figure 4.17, show similar results to the temperature property. However, the glider does provide more distinct positive impact on the velocity. Glider, mooring and satellites all have similar positive impact on the deeper layer of Mamala Bay, across the region. HF radar has a more dominant positive impact especially off the east coast of Barbers Point and Diamond Head. This shows that the surface constraint provided by the HF radar has an important influence through depth, more than previously considered.

4.3 OTEC at Plume Depth, 215m

At the OTEC plume depth, density and velocity were assessed because being able to accurately forecast these parameters at the plume is more critical for OTEC operations. Mean temporal density RMS, figure 4.18, for the all observations case is 0.069kg/m³. Withholding the satellites or HF radar raises the RMS to 0.077kg/m³ and the glider raises the RMS further to 0.081kg/m³. The greatest impact came from withholding the mooring which raise the RMS to 0.089kg/m³. The background RMS was 0.108kg/m³. The mean correlation for the all observations case is 0.83. When the glider is withheld, the correlation drops to 0.76, and without the satellites, it drops to 0.751. Removing the mooring, the correlation is 0.747. The most influential observation on the correlation was HF radar with a correlation of 0.71. The background correlation is 0.51. HF radar and SST have slightly greater impact than

the glider and mooring but across the temporal forecast period different observations are shown to have the greatest impact throughout. Over the full 96 hours, the RMS shows an increasing trend, and the skill, a similar decreasing trend, suggesting the forecast quality degrades over time.

The spatial plume density, Figure 4.19, shows HF radar is still providing a valuable constraint on the density at the OTEC site, at 215m even though it samples the ocean at the surface. The mooring also shows valuable positive impact. The glider is able to constrain the model density, suggesting when it samples below the thermocline near 150m, it is effectively constraining the model state. The satellites also have a positive impact, although of a smaller scale.

The temporal velocity forecast RMS and correlation at the OTEC plume depth site, Figure 4.20, shows HF radar as the dominant observing sensor again. The mean temporal results for RMS with all observations is 0.08m/s. When the glider is withheld, the RMS is .09m/s. Withholding satellites or mooring raises the RMS to 0.102m/s and withholding the HF radar produces an RMS of 0.11m/s. The background RMS is 0.15m/s. The mean correlation for the all observations case is 0.85. When the glider is removed, it drops to 0.75, and withholding the mooring it is slightly lower at 0.74. Withholding satellites produces a correlation of 0.71, but the forecast correlation when HF radar is withheld drops to 0.69, The background correlation is 0.21. HF Radar and satellite data show a higher impact than the glider and mooring. The spatial RMS for the OTEC velocity, Figure 4.21, shows HF radar and satellites to have similar impacts and the mooring and glider have similar impacts though at a lower magnitude than the HF radar and satellites.

4.4 Analysis of results

Overall, satellites had the greatest impact on the temperature forecasts. SST has the best spatial coverage, covering the entire grid, though only sampling it two times per day. While its temporal constraint is more lacking than the other sensors the spatial coverage of the surface temperatures is enough to constrain the model well. HF radar has the greatest impact on velocity forecasts. It has moderate spatial coverage, relative to the SST satellites, but it samples the grid every 3 hours providing more thorough temporal coverage. This is enough to constrain the model well in the upper 70m and in Mamala Bay in the lower 70-150m range. In fact, the radar has a stronger impact on temperature at depth than the satellites do, suggesting the velocity constraint is significant. The glider and mooring have even better temporal coverage sampling every five minutes and one hour respectively, but their spatial coverage is not enough to constrain the temperature or velocities across the entire model as well as HF radar and satellites.

In this study, all observations could be fully assimilated and all had a noticeable positive impact on the forecasts. Bouttier and Kelly (2001) also found that in data-poor areas, sparse observing systems were still better than none at all and improved the forecast, even if only in the short range. In an area like Oahu regional grid with such dynamic variability, a short range forecast is valuable and sparse observing systems can improve the forecast as well. In this experiment period, the synthetic seaglider was transiting throughout. One could presume that even a short term glider sampling period would still improve the local forecast, especially near the glider route.

Figures

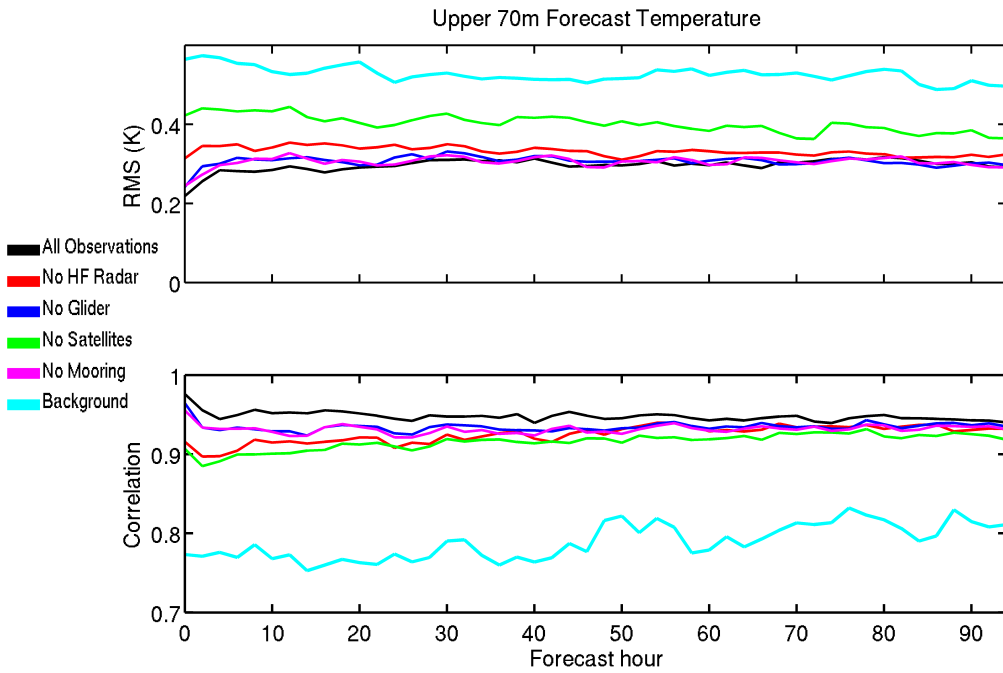


Figure 4.1: Median RMS (top) and correlation (bottom) of temperature in the upper 70m, through the forecast cycle between each forecast OSSE and the state estimation when all observations were assimilated. Median computed for 41 four day forecasts. Cyan is RMS with Background (when no assimilation was applied). Black is forecast case when all observing systems were assimilated (best case). Red is case when HF Radar was withheld. Green is case when satellites were withheld. Magenta is case when mooring is withheld. Blue is case when glider is withheld. These colors apply for all temporal comparisons in this chapter. The temporal forecast RMS and correlation are also computed the same way throughout the results.

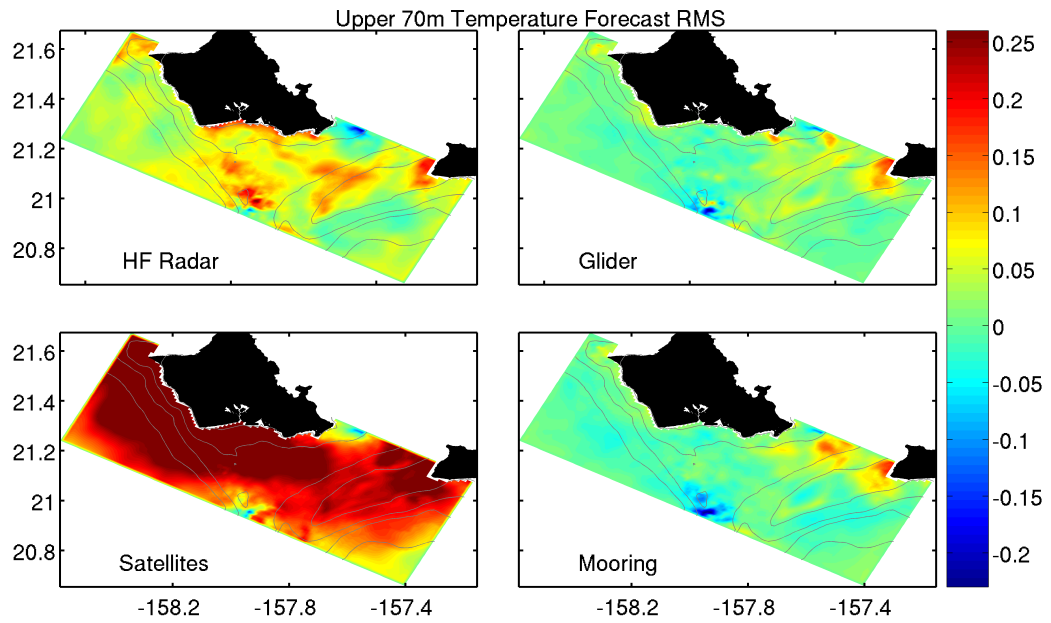


Figure 4.2: Mean Spatial RMS impact of temperature in the upper 70m. Each subplot represents the impact of the sensor labeled. Impact described in section 3.6.

Upper 70m Temperature Forecast Correlation Impact

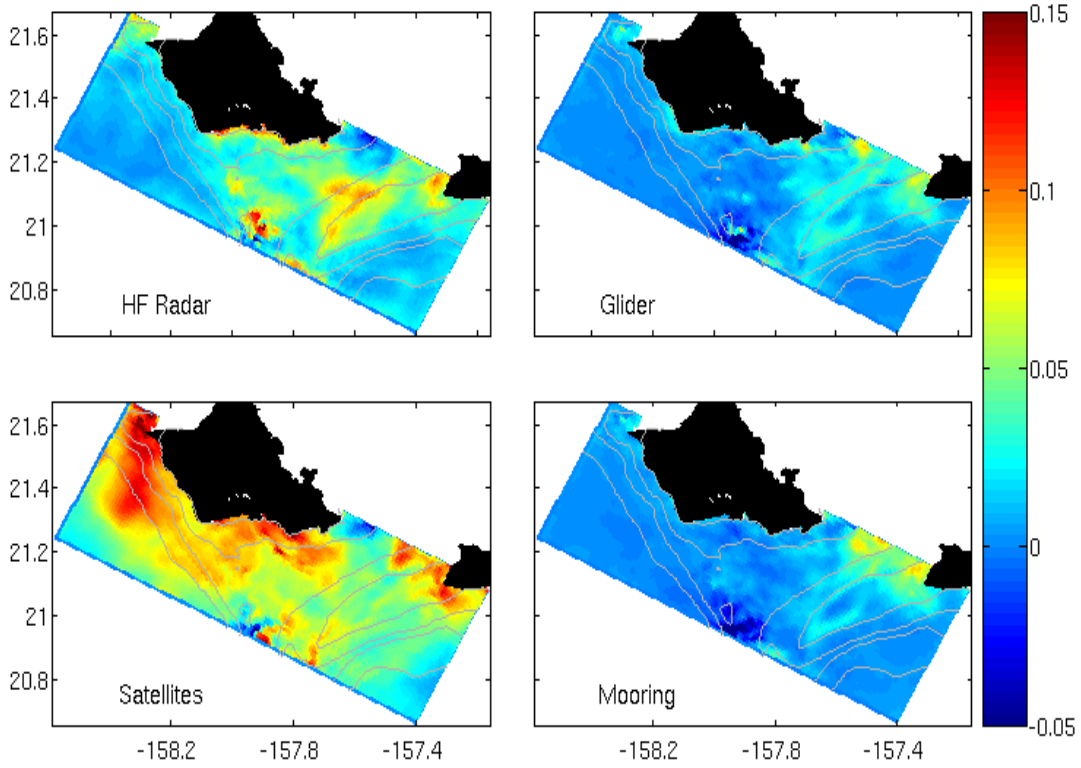
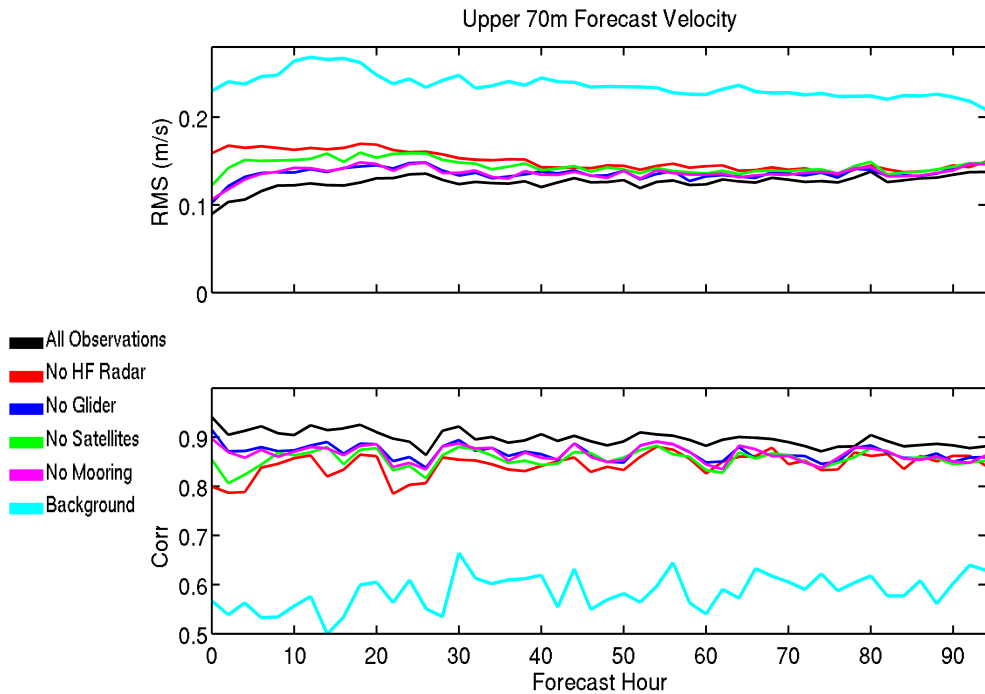


Figure 4.3: Spatial correlation impact calculated for each spatial point through six month experiment period between each case and the state estimation when all observations were assimilated. Each subplot represents the impact of the sensor labeled. Impact described in section 3.6.



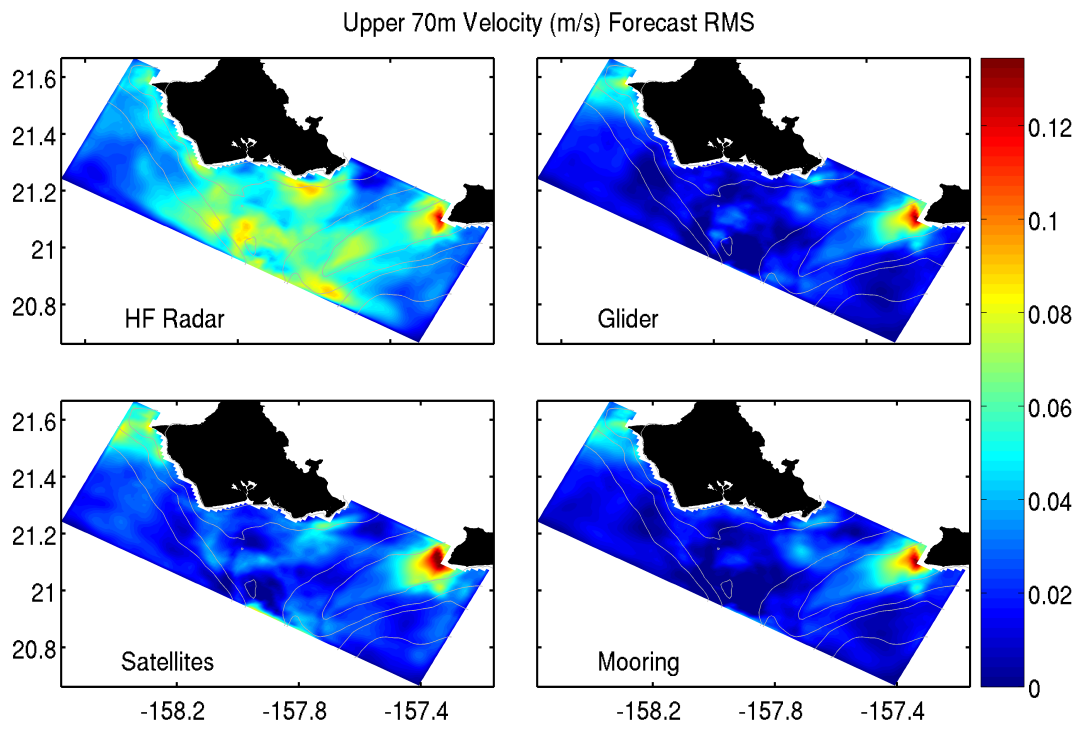


Figure 4.5: Spatial RMS impact of velocity in the upper 70m.

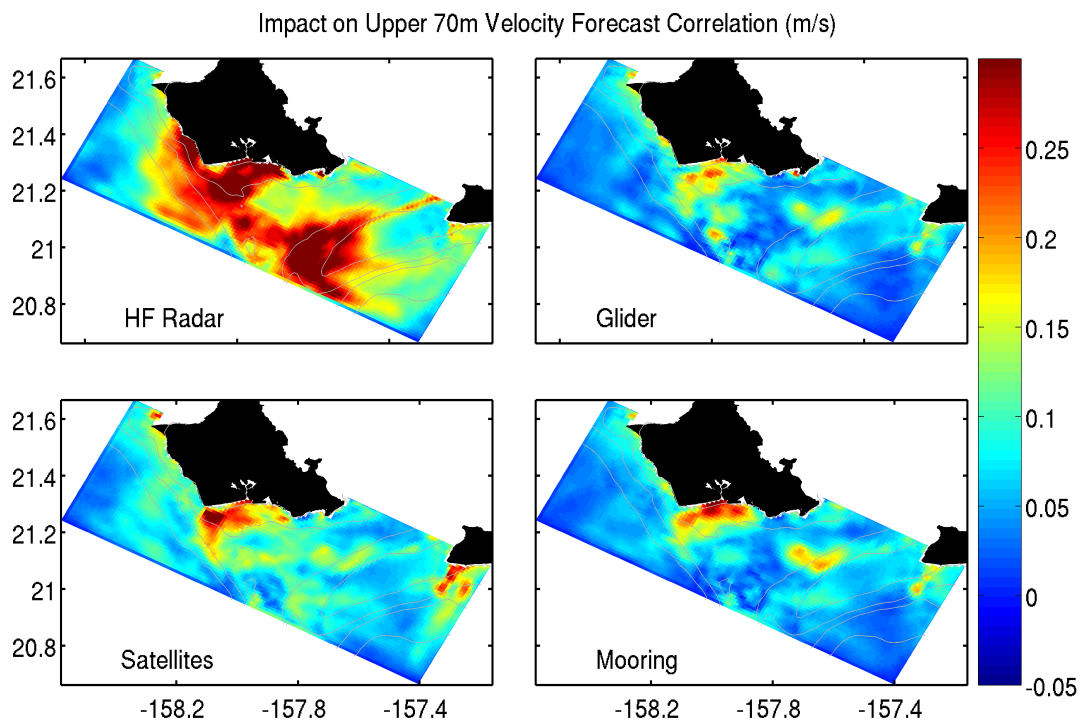


Figure 4.6: Spatial correlation impact of velocity in the upper 70m.

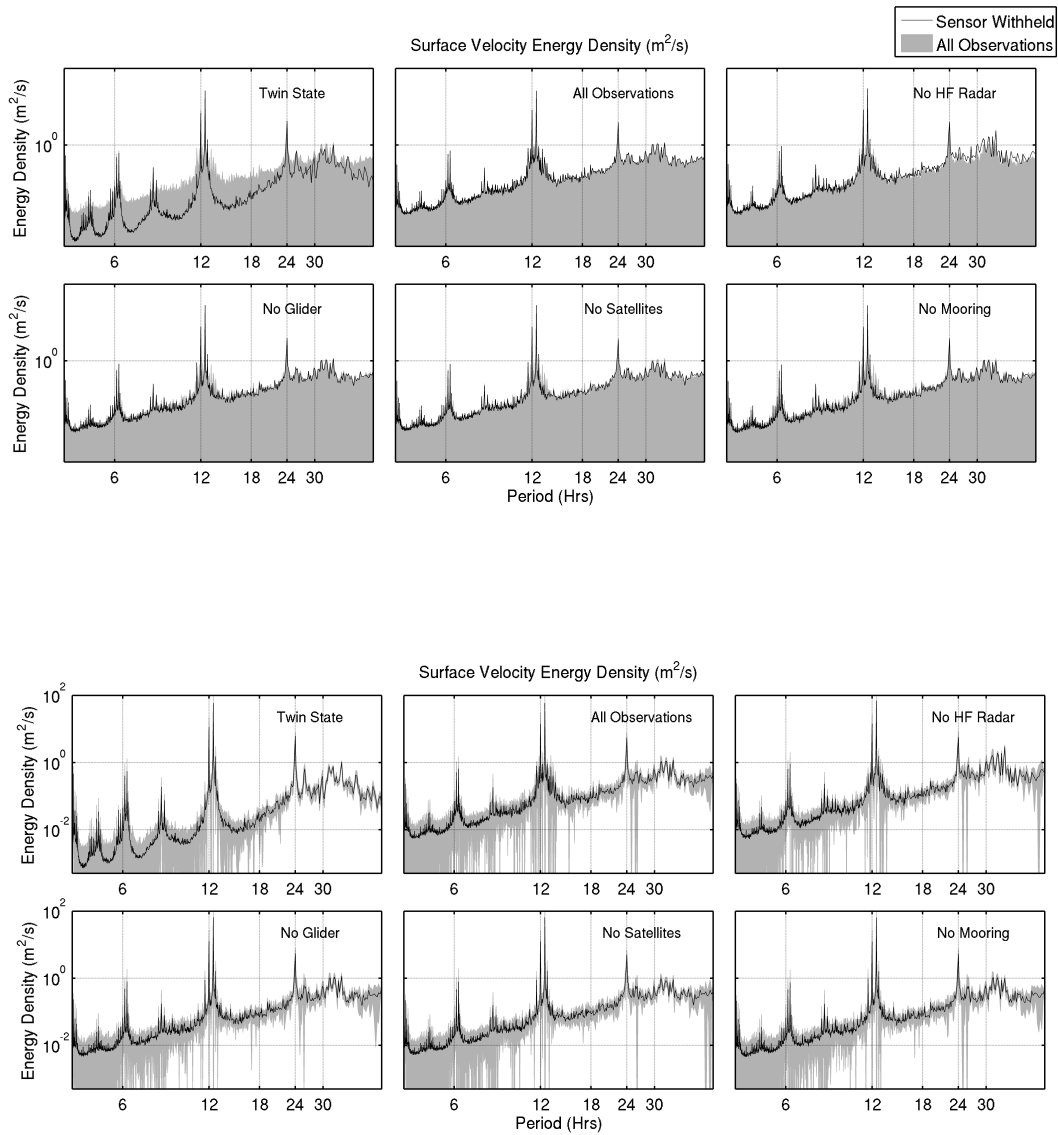


Figure 4.7: Surface velocity Energy Density computed from state estimation for each case. For each subplot, the sensor listed represents the sensor withheld from that state estimation. The top left subplot represents the twin state, from which the observing systems were sampled. The top middle plot represents the best case capture of energy density, when every observing system is included in the state estimation. For the top set of plots, the shaded grey represents the best case scenario to show relative comparison. For the bottom set of plots, error bars are shown in grey on either side of each energy density spectrum.

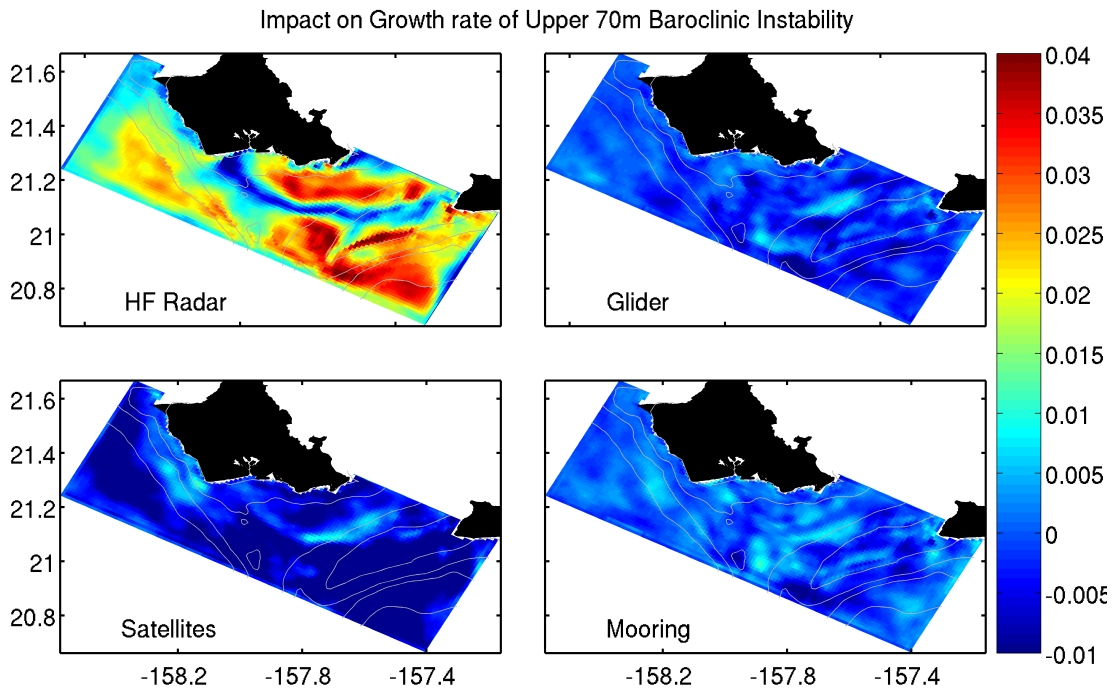


Figure 4.8 Impact of each sensor on growth rate of upper 70m baroclinic instability. Negative values of impact indicate the sensor is negatively influencing the model's measurement of growth rate.

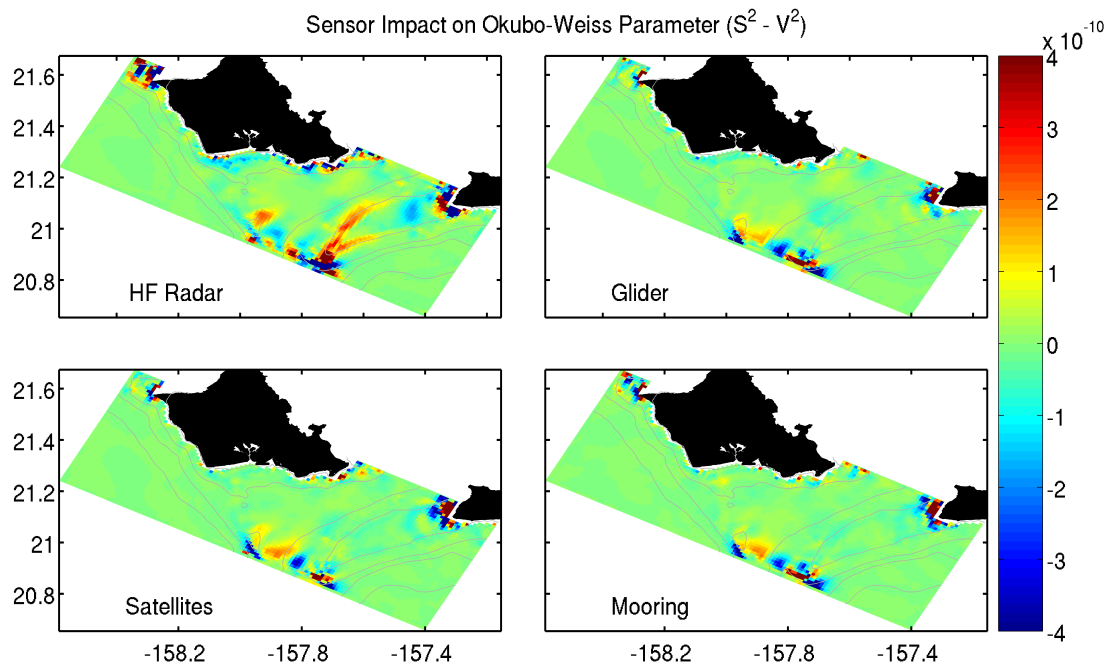


Figure 4.9 Impact of each sensor on Okubo-Weiss parameter.

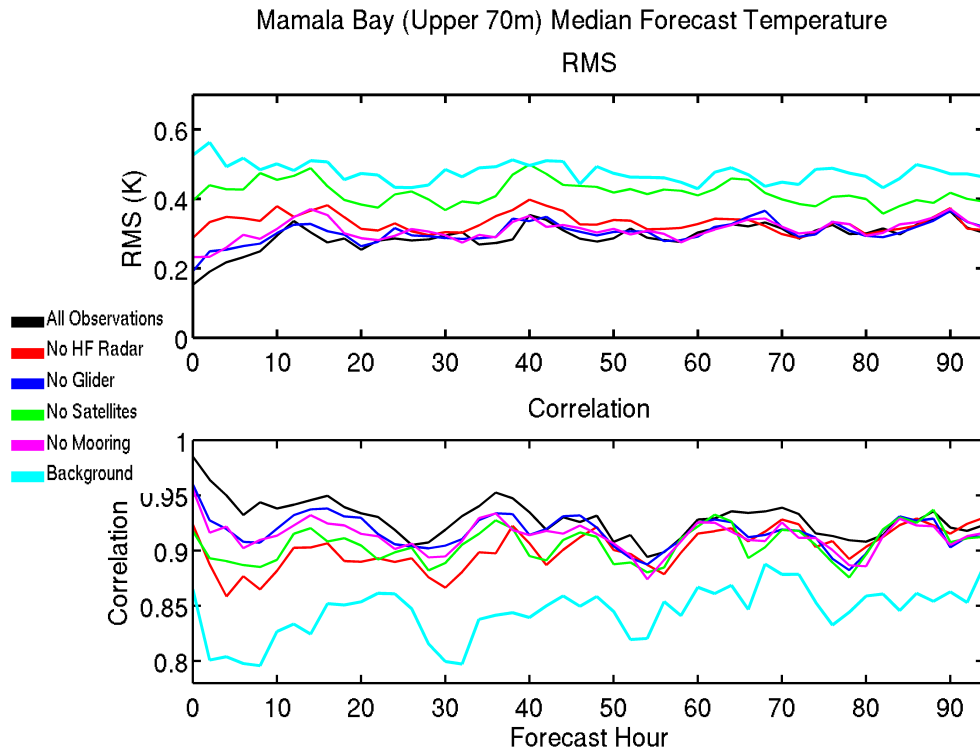


Figure 4.10: Median RMS (top) and correlation (bottom) of temperature in the upper 70m of Mamala Bay.

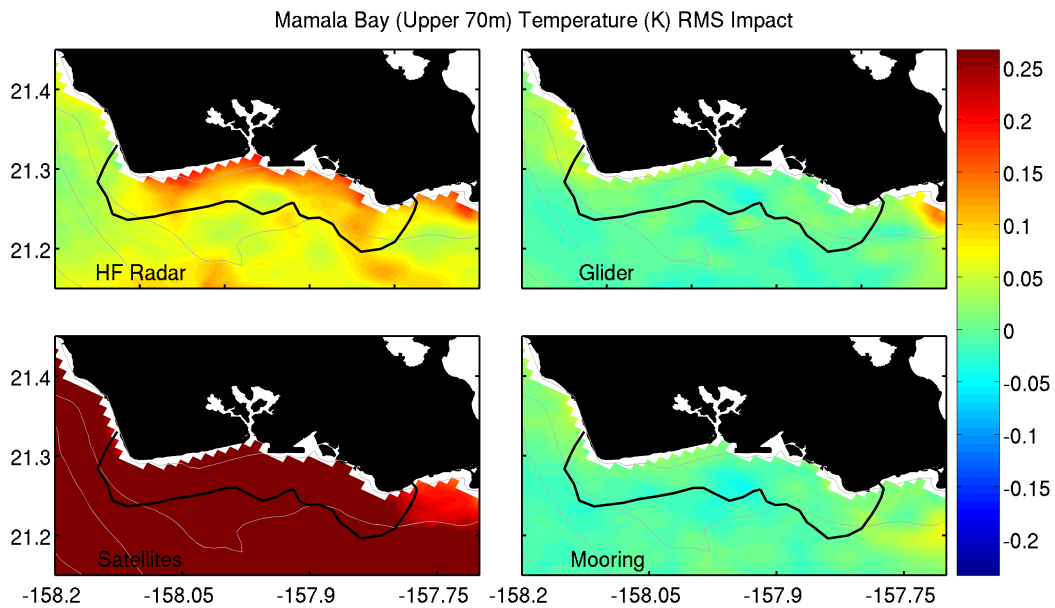


Figure 4.11: Spatial RMS impact of temperature in the upper 70m of Mamala Bay.

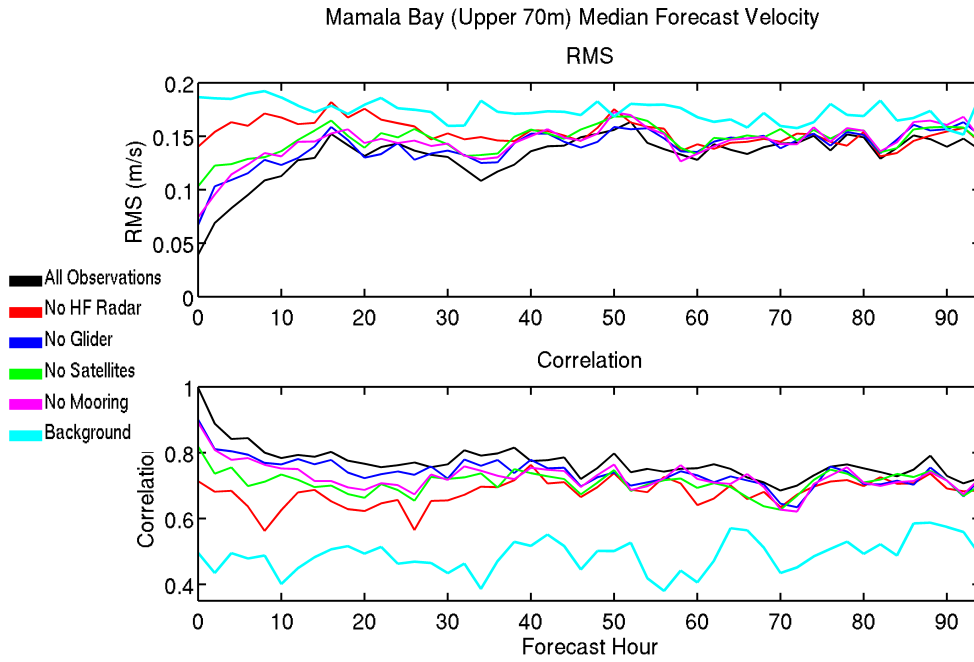


Figure 4.12: Median RMS (top) and correlation (bottom) of velocity in the upper 70m of Mamala Bay.

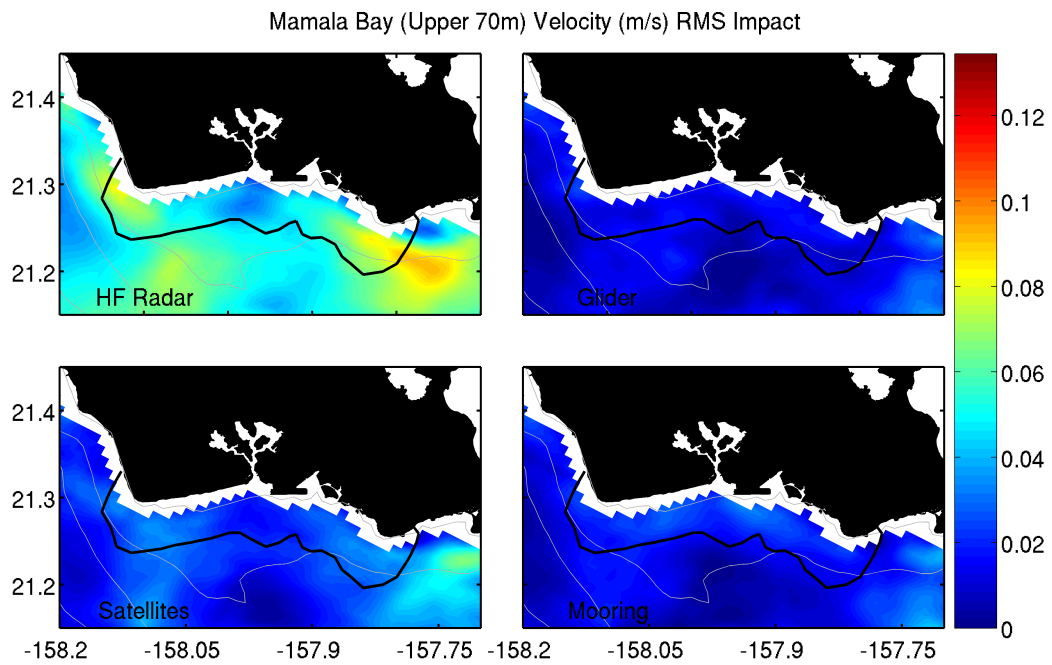


Figure 4.13: Spatial RMS impact of velocity in the upper 70m of Mamala Bay.

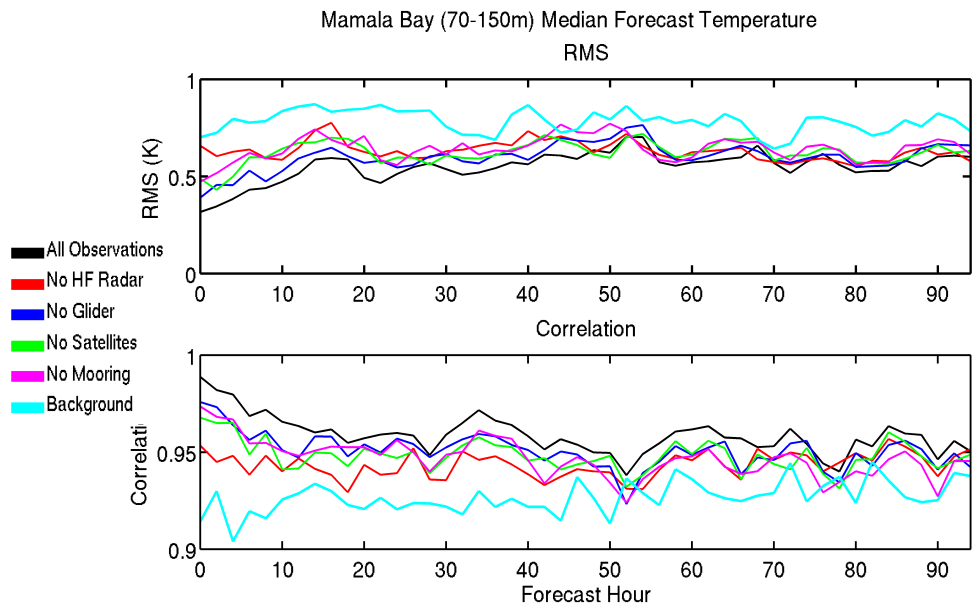


Figure 4.14: Median RMS (top) and correlation (bottom) of temperature in the 70-150m depth layer of Mamala Bay.

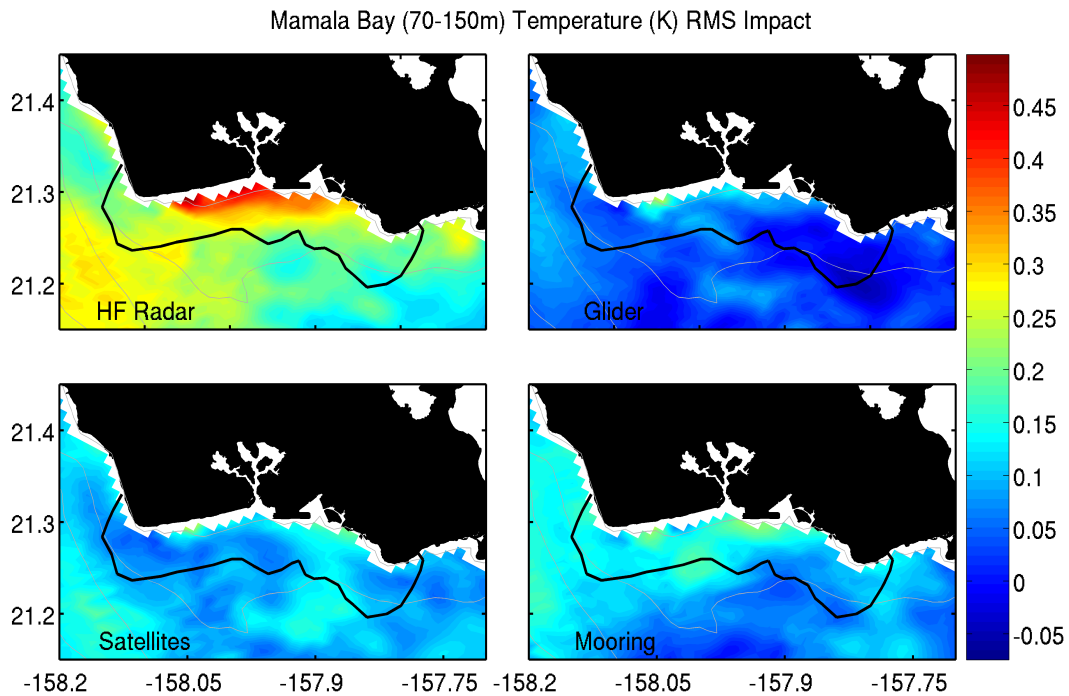


Figure 4.15: Spatial RMS impact of temperature in the 70-150m depth layer of Mamala Bay.

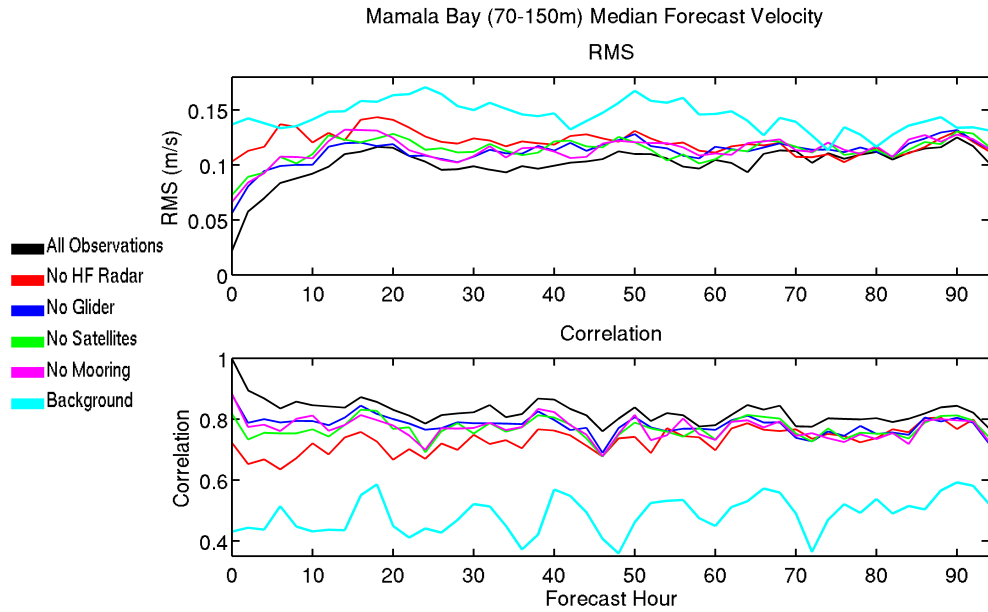


Figure 4.16: Median RMS (top) and correlation (bottom) of velocity in the 70-150m depth layer of Mamala Bay.

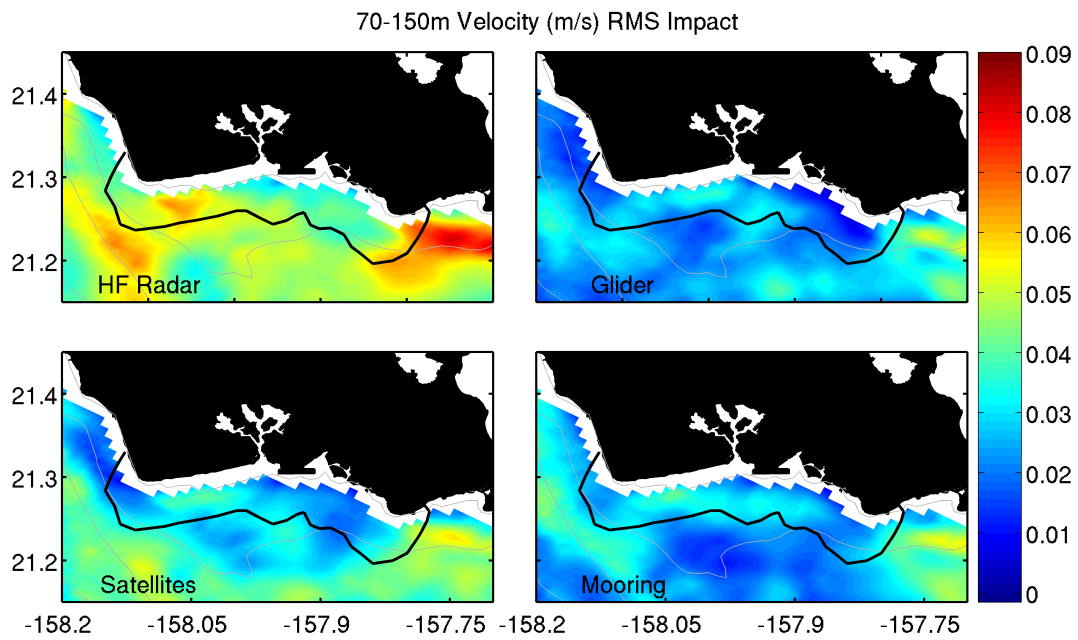


Figure 4.17: Spatial RMS impact of velocity in the 70-150m depth layer of Mamala Bay.

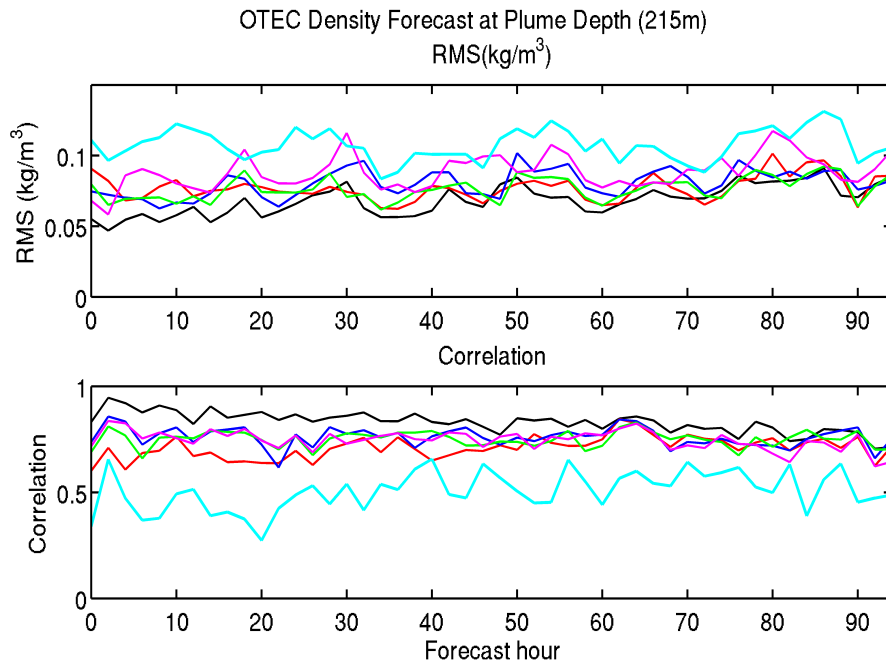


Figure 4.18: Median RMS (top) and correlation (bottom) of density at the plume depth of the OTEC area.

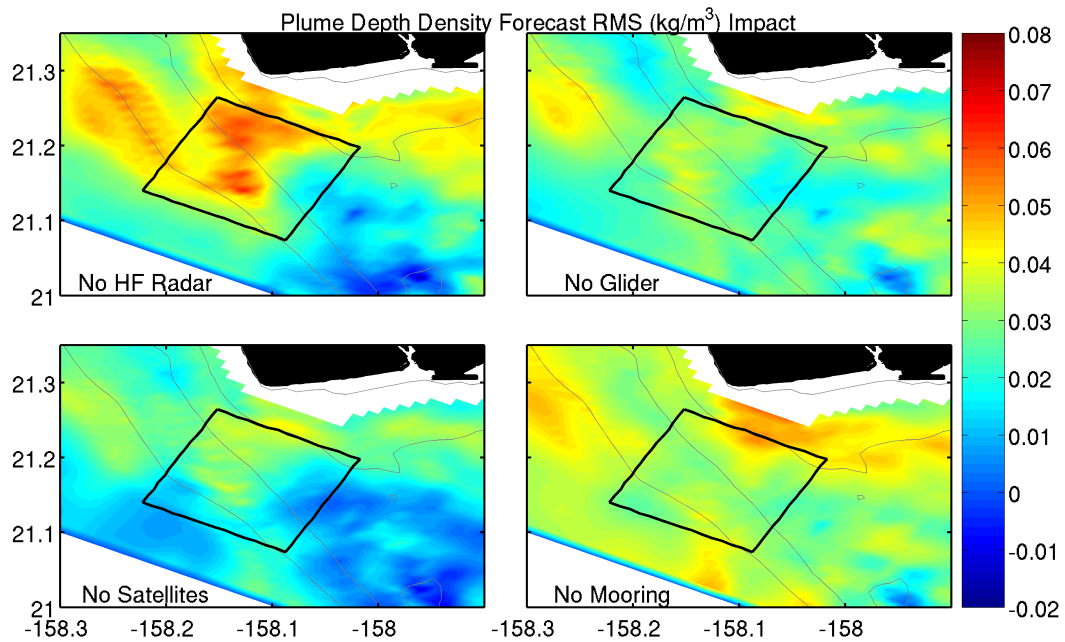


Figure 4.19: Spatial RMS impact of density at the plume depth of the OTEC area.

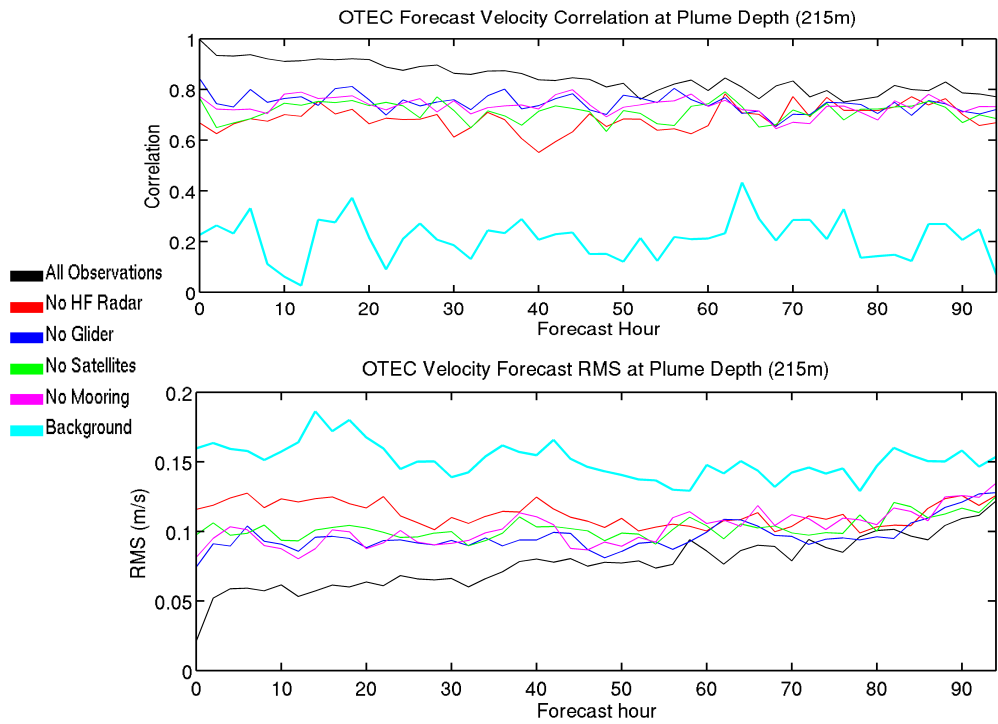


Figure 4.20: Median RMS (top) and correlation (bottom) of velocity in the upper 70m of the OTEC area.

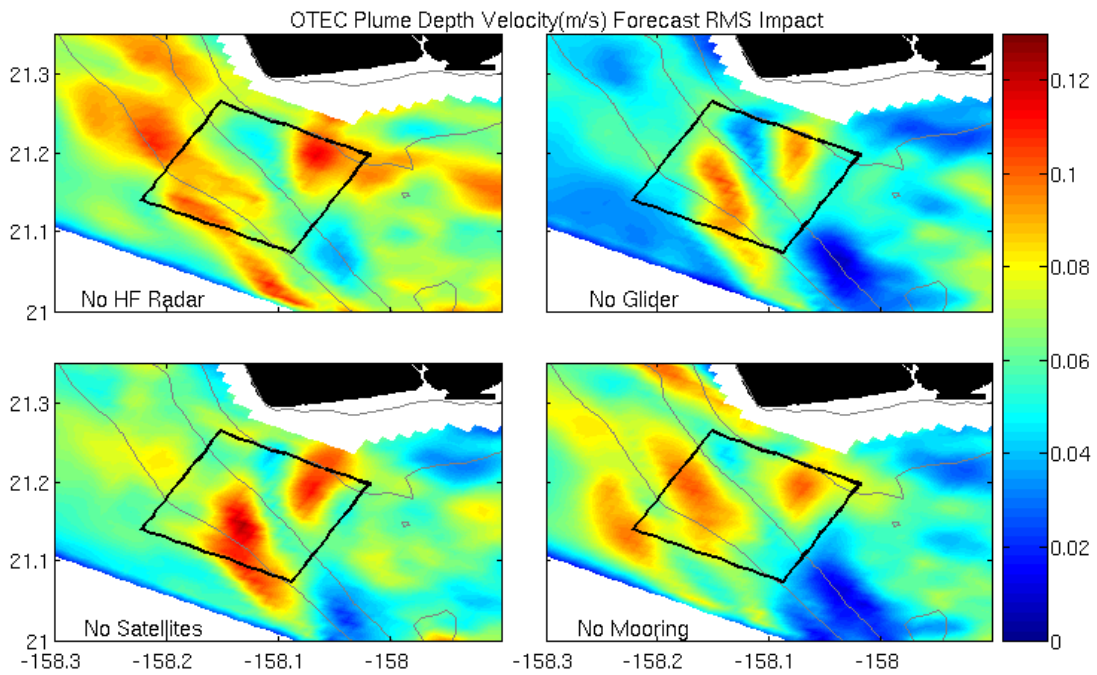


Figure 4.21: Spatial RMS impact of velocity at the plume depth of the OTEC area.

Chapter 5

Conclusion

In this study we compared four high-resolution ROMS simulations of ocean dynamics in the Oah'u regional ocean model. The focus of our study is the resulting impact of withholding observing systems from the state estimation and forecast process. Comparison between the model results shows that all observing systems have some positive impact on model forecasts.

This observing system experiment was set in an extremely dynamic region. This challenging region has dynamic tidal activity, barotropic-to-baroclinic conversion, internal wave activity, and variable topography with steep sloping features unlike simpler regions elsewhere in the world. The cases considered in this experiment found that while the region is under sampled, all observing systems have some positive impact on model forecasts, and some more than others.

HF radar was shown to be a crucial observing system for model forecasting by constraining the model at both the surface and at depth. It showed particularly strong impacts on the northern side of Penguin Bank and across the radar coverage area. Satellites also showed significant impact on forecasts across the region. Correlation impact figures revealed the satellites provide particular constraint on model forecasts in the shadow zone of the islands. Well placed gliders and mooring can be useful in forecasting near high dynamical localized areas, though they have less range of influence than the spatial coverage of the HF radar and satellite observing systems. In the Ka'iwi Channel, the glider and mooring each showed positive impact as a constraint across the major open boundary flow into the model.

This experiment is not designed to assess sensor effectiveness but rather sensor data effectiveness for ROMS model forecasts. In conducting the OSSE in such a dynamic region, it was important to capture all the dynamical influences as well as possible. In future work, all tidally influenced observation sensors should have a low pass filter applied to them and then tides from the model can be synthesized with the observation to eliminate any introduction of tidal errors. Comparing the model to as much observational data as possible allows for continued calibration and refining of the model solution to best replicate the dynamics in the region.

Coastal forecasting can be improved with more observing sensors available and since these types of experiments can be successfully carried out in the dynamic and variable environment described by ROMS, this technique should be as effective in other more acquiescent regions. Overall this project showed observing systems improve a model forecast even with extraordinary dynamic activity already being negotiated with in the model.

References

- Arango, H. "Modeling and Data Assimilation in the Philippine Archipelago,"
Philippines Straits Dynamics Experiment Workshop, Honolulu, HI, August
27, 2009
- Barth, J.A., 1994, Short-wavelength instabilities on coastal jets and fronts, *Journal of Geophysical Research*, vol. 99, No. C8, 16095-16115.
- Barrick, D.E., Evans, M.W., Weber, B.L., 1977, Ocean surface current mapped by radar, *Science*, 198:138-144
- Bouttier, F, Kelly, G., 2001 Observing systems experiments in the ECMWF 4D-Var data assimilation system, *Q.J.R Meteorol Soc.* 127 p.1469-1488
- Broquet, G., Edwards, C.A., Moore, A.M., Powell, B.S., Veneziani, M., Doyle, J.D. 2009. Application of 4D-Variational data assimilation to the California Current System. *Dynamics of Atmospheres and Oceans*, 48, 69-92.
- Calil, P.H.R, Richards, K.J., Jia, Y., Bidigare, R.R., 2008, Eddy activity in the lee of the Hawaiian Islands. *Deep-Sea Research II*, 55, 1179-1194.
- Carter, G.S., Merrifield, M.A., Becker, J.M., Katsumata, K., Gregg, M.C., Luther, D.S., Levine, M.D., Boyd, T.J., Firing, Y.L.. 2008. Energetics of M_2 Barotropic-to-Baroclinic Tidal Conversion at the Hawaiian Islands, *Journal of Physical Oceanography*, Vol 38, 10, 2205-2223.
- Carter, G.S. Gregg, M.C. 2006, Persistent Near-Diurnal Internal Waves Observed above a Site of M_2 Barotropic-to-Baroclinic Conversion, *Journal of Physical Oceanography*, Vol. 36, 1136-1147
- Cass, J.L., 2010. High Frequency Observations of Tides and Currents South of O'ahu, Unpublished MS thesis, University of Hawai'i.
- Chavanne, C., P. Flament, R. Lumpkin, B. Dousset, A. Bentamy. 2002 Scatterometer observations of wind variations induced by oceanic islands: Implications for wind-driven ocean circulation. *Can. J. Remote Sensing*. 28, 466-474.
- Chen, C., Malanotte-Rizzoli, P., Wei, J., Beardsley, R.C., Lai, Z., Xue, P., Lyu, S., Xu, Q., Qi, J. and Cowles, G. 2008. Validation of Kalman filter for coastal ocean problems: An experiment with FVCOM. *Journal of Geophysical Research*, 114, C05011, 17.
- Colossi, J.A., Munk, W., 2006. Tales of the Venerable Honolulu Tide Gauge. *Journal of Physical Oceanography*, 36, 967-996.

- Courtier, P., Thépaut, J.N., Hollingsworth, A., 1994. A strategy for operational implementation of 4D-Var, using an incremental approach. *Quarterly Journal of the Meteorological Society*, 120, 1367-1387.
- Cummins, P. F., Oey, L.Y. 1997: Simulation of barotropic and baroclinic tides off northern British Columbia. *J. Phys. Oceanogr.*, 27, 762–781.
- Eriksen, C.C., Osse, T.J., Light, R.D., Wen, T., Lehman, T.W., Sabin, P.L., Ballard, J.W., Chiodi, A. M., 2001, Seaglider: A Long-range Autonomous Underwater Vehicle for Oceanographic Research, *IEEE J Oceanic Eng.* 26:424-436.
- Essen, H.H., Gurgel, K.W. Schlick, T., 1999, Measurement of ocean wave height and direction by means of HF radar: an empirical approach, *German J. of Hydrography*, 51(4):369-383.
- Essen, H.H., Gurgel, K.W., Schlick, T., 2000, On the Accuracy of Current Measurements by Means of HF Radar, *IEEE J Oceanic Eng.* 25(4):472-480.
- Garrett, C., Kunze, E., 2007, Internal Tide Generation in the Deep Ocean, *Annual Review of Fluid Mechanics*, 39, 57-87.
- Gurgel, K.W., Essen, H.H., Schlick T., 2001, The University of Hamburg WERA HF Radar – Theory and Solutions, First International Radiowave Oceanography Workshop ROW 2001 *Proceedings*, 1-7.
- Holloway, P.E., Merrifield, M.A. 1999, Internal tide generation by seamounts, ridges and, islands, *Journal of Geophysical Research*, 104, C11, p.25,937-25,951.
- Lacarra, J.F., Talagrand, O., 1988. Short-range evolution of small perturbations in a barotropic model. *Tellus*, 40A, 81-95.
- Le Dimet, F. X., Talagrand, O., 1986. Variational algorithms for analysis and assimilation of meteorological observations: theoretical aspects. *Tellus*, 38A, 97-110.
- Lumpkin, C., 1998. Eddies and Currents of the Hawaiian Islands. PhD dissertation, School of Ocean and Earth Sciences and Technology, University of Hawai'i Manoa.
- Moore, A.M., Arango, H.G., DiLorenzo, E., Cornuelle, B.D., Miller, A.J., Neilson, D.J.. 2004. A comprehensive ocean prediction and analysis system based on the tangent linear and adjoint of a regional ocean model, *Ocean Modeling*, 7, 227-258.

- Shchepetkin, A.F., McWilliams, J.C., 2005. The Regional Oceanic Modeling System: a split-explicit, free-surface, topography-following-coordinate ocean model. *Ocean Modeling* 9, 347-404.
- Pawlowicz, R. Beardsley, B. Lentz, S., "Classical tidal harmonic analysis including error estimates in MATLAB using T_TIDE", *Computers and Geosciences* 28 (2002), 929-937
- Powell, B.S., Arango, H.G., Moore, A.M., DiLorenzo, E., Milliff, R.F., Foley, D., 2008. 4DVAR data assimilation in the Intra-Americas Sea with the Regional Ocean Modeling System (ROMS). *Ocean Modeling* 23, 130-145.
- Qiu, B., Koh, D.A., Lumpkin, C. Flament, P., 1997. Existence and Formation Mechanism of the North Hawaiian Ridge Current, *Journal of Physical Oceanography*, 27, p.431-444.
- Rudnick, D.L., Eriksen, C.C., Fratantoni, D.M., Perry, M.J., 2004, Underwater Gliders for Ocean Research, *J. Marine Tech. Soc.*, 38(2), 73-84.
- Stewart, R.H., Methods of Satellite Oceanography, San Diego, CA: Scripps Institute of Oceanography, 1985.
- Undén, P. Kelly, G. LeMeur, D. Isaksen, L., 1997, Observing System experiments with the 3D Var assimilation system. ECMWF Research Department Technical Memorandum no. 244. Available from ECMWF, Shinfield Park, Reading RG2 9AX, UK
- Vallis, G.K., *Atmospheric and Ocean Fluid Dynamics: Fundamentals and Large-Scale Circulation*, New York, Cambridge University Press, 2006.
- Wang, N., Gerritsen, F., 1995, Nearshore circulation and dredged material transport at Waikiki Beach, *Coastal Engineering*, 24: 315-341
- Weaver, A.T., Vialard, J., Anderson, D.L.T., 2003. Three and four dimensional variational assimilation with a general circulation model of the tropical pacific ocean. Part I: Formulation, internal diagnostics, and consistency checks. *Monthly Weather Review* 131, 1360-1378.
- Weller, R.A., Rudnick, D.L., Pennington, N.J., Trask, R.P., Valdes, J.R., 1990, Measuring upper ocean variability from an array of surface moorings in the subtropical convergence zone. *Journal of Atmospheric and Oceanic Technology*. Vol 7. p68-84.
- Xie, S.P., Liu, W.T., Liu, Q., Nonaka, M., 2001, Far-Reaching Effects of the Hawaiian Islands on the Pacific Ocean-Atmosphere System. *Science*, Vol 292, p.2057-2060.